
# Characterization of Multipixel Avalanche Photodiodes

Master Thesis in Nuclear Physics

by

Hege Austrheim Erdal

University of Bergen
Department of Physics and Technology
June 2009

# Acknowledgments

First of all I would like to thank my supervisor Professor Dieter Röhrich for giving me the opportunity to work on this project. The two years spent in the nuclear physics group here in Bergen has been very interesting. Thank you for all the help I have received and the clarifying conversations.

A thank you goes also to my bi-supervisor Dr. Scient. Renate Grüner. You are always so supportive and helpful when I have asked for help, and I am very grateful for that.

Thanks to Dominik Fehlker and Njål Brekke, I am not sure what I would have done without the two of you! Thank you for all those enlightning discussions and all the help I have received. Professor Gerald Eigen and Dr. Scient. Heidi Sandaker has also been of a great help this last year. Thanks to Werner Olsen for helping me get started on the project.

Thanks to Alexander Tadday for taking care of me while I was in Germany, and also for all the help I received while being there. I learned a lot during those two weeks.

A very special thanks to my best friend during these 5 years, Jenny Louise Luneng. You have always been there for me, and I am very grateful for that.

I would also like to thanks to all the people I have met during my years here at the institute, I could not have gone through all those hours of studying without you. This goes especially to the 5th floor and the nuclear physics group.

Last, but not least, I would like to thank my family, who has always encouraged and supported me to study.

Bergen, 2nd June, 2009

Hege Austrheim Erdal

# Summary

The overall objective of this thesis has been to characterize different types of Geiger mode avalanche photodiodes. Due to the growing variety of these detectors, it is important to develop knowledge about the different types. The different types of photodetectors have in addition internal differences, which makes it important to characterize each individual sample.

The subatomic group at the Department of Physics, University in Bergen, has a long history of experience with calorimeters. Unfortunately the detector laboratory burned down two years ago. Therefore, the setup for measuring the characteristics of calorimeters and their read-out had to be built up from scratch. This has mainly been done in cooperation with senior engineer Dominik Fehlker and PhD-student Njål Brekke. A lot of time has then been used to understand the readout system and data-acquisition system, i.e. to reduce noise and to come up with a setup which makes it easy to characterize different photodetector with respect to dark current, dark rate and absolute gain.

Four types of detectors have been tested, two MultiPixel Avalanche Photodiodes (MAPD) from Zecotek and Dubna and two MultiPixel Photon Counters (MPPC) from Hamamatsu. They differ in gain and dynamical range, which makes them interesting for different applications.

The high dynamical range of the MAPDs makes them particularly interesting for calorimeters. Here the the energy of an electromagnetic or a hadronic cascade are measured. Several projects are looking into the use of different MAPDs in calorimeters, among them are the Projectile Spectator Detector (PSD) which will be located at NA61/SHINE at CERN.

The MPPCs have a smaller dynamical range, but exhibit on the other hand a very high gain compared to the MAPDs. This makes them interesting in applications where low photon energies are detected. This is the case for Positron Emission Tomography (PET), a nuclear medical imaging technique that produce a three-dimensional image of biochemical processes in the body. It detects photon-pairs emitted indirectly from a positron emitting nuclei. In addition, these MPPC devices are very fast, which makes them interesting for Time-of-Flight (ToF) PET. ToF PET uses the time difference in arrival time of the two photons in a coincidence detection, which among other things will reduce the statistical noise in the medical image.

The absolute gain has been recorded for different samples of the MPPCs. The gain ranged between (0.1-1.4) $\cdot 10^6$, depending on the reverse bias voltage and temperature. For the two different types of MPPC, the gain dependence on the voltage has been recorded to be 4.4% and 7% when increasing the bias voltage with 0.1 V from the recommended bias voltage. The gain dependence on temperature has been recorded to be 2.2% and 3.8% when increasing the temperature from $24^o$C to $25^o$C.

The dark rate has been recorded for the same MPPC samples, showing results between $10^4$ - $2 \cdot 10^7$ Hz, depending on the reverse bias voltage.

# Contents

# Chapter 1

# Introduction

A particle, be it a hadron, an electron or a photon, entering a detector will interact with the material. In the case of a photon entering an crystal, an electromagnetic cascade will be created. As a result, the crystal will be excited, i.e. electron-hole pairs will be created. These pairs recombine at localized recombination centers by emitting visible light. Different photodetectors are used for photon detection. A well known photodetector is the PhotoMultiplier Tube (PMT) and the Avalanche PhotoDiode (APD). The last years a new kind of photodetector has been developed, the Multipixel Avalanche PhotoDiodes (MAPD). It is a pixelated device, with each pixel being a semiconductor diode operated in Geiger Mode. In addition to matching the gain of the PMTs, the MAPDs have the advantage of being insensitive to magnetic field. This makes them interesting for many applications.

The subatomic group at the Department of Physics, University in Bergen, has a long history of experience with calorimeters. Unfortunately, the detector laboratory burned down two years ago. Therefore, the setup for measuring the characteristics of calorimeters and their read-out had to be built up from scratch. This was done mostly in co-operation with senior engineer Dominik Fehlker and PhD-student Njål Brekke. A lot of time has then been used to understand the readout and data-aquisition system, i.e. to reduce noise and to come up with a setup that makes it easy to characterize different photodetectors with respect to gain, dark current and dark rate. The aim of this thesis is twofold: (1) to demonstrate the status of the capabilites for characterizing photodetectors and (2) to compare the performance of two types of novel photodetectors: MAPDs and MPPCs.

The introduction deals with the interaction of charged particles and photons with matter. Chapter 2 focuses on the detection principles of various detectors for visible photons, introducing Multipixel Avalanche Photodiodes. Chapter 3 shortly describes two typical applications for the MAPDs: a hadronic calorimeter for projectile spectators (NA61, CBM) and a PET

detector. The experimental setup used in the thesis is described in Chapter 4, followed by a presentation of the measurements of the characteristic properties of two different types of novel photodetectorts: MAPDs and MPPC (Chapter 5). The photodetectors will be measured with respect to absolute gain, dark current, dark rate and linearity. A summary of the results and an outlook on further measurements are given in Chapter 6.

## 1.1 Energy Loss of Charged Particles

Charged particles passing through matter will interact in different ways, depending on the type of charged particle, the matter it travels through and the speed of the particle. The main interactions of different charged particles are described in the following.

### 1.1.1 Energy loss of heavy particles

A charged particle that traverses a layer of material can interact electromagnetically with the material via inelastic scatterings. This will cause an ionization or excitation of the atoms. The energy loss $dE$ per unit path length $dx$ is described by the Bethe-Bloch formula [1]:

$$-\frac{dE}{dx} = 2\pi N_A r_e^2 m_e c^2 \rho \frac{Z}{A}\frac{z^2}{\beta^2}\left[ ln(\frac{2m_e\gamma^2 v^2 W_{max}}{I^2}) - 2\beta^2 - \delta - 2\frac{C}{Z}\right], \tag{1.1}$$

where $N_A$ is Avogadro's number, $m_e$ and $r_e$ is the electron mass and classical radius. $\rho$, Z and A is the density, atomic number and atomic weight of the absorbing material. z is the charge of incident particle in units of e. I is the mean excitation potential, $\delta$ is the density correction while C is the shell correction. $W_{max}$ is the maximum energy transfer in a single collision, and is produced by a head-on or knock-on collision. If the incident particle has a mass M, $W_{max}$ is given by [1]

$$W_{max} = \frac{2m_e c^2(\beta\gamma)^2}{1 + 2\frac{m_e}{M}\sqrt{1+(\beta\gamma)^2} + (\frac{m_e}{M})^2}\ . \tag{1.2}$$

Also, if M>>$m_e$, then $W_{max} \cong 2\ m_e\ c^2\ (\beta\gamma)^2$. For all practical purposes in high-energy physics dE/dx in a given material is a function only of $\beta$ (a minor dependence on M at the highest energies is introduced through $W_{max}$).

### 1.1.2 Energy loss by electrons and positrons

As Fig 1.1 shows, low energy electrons and positrons can lose energy by processes like Møller scattering, Bhabha scattering and $e^+$ annihilation, but

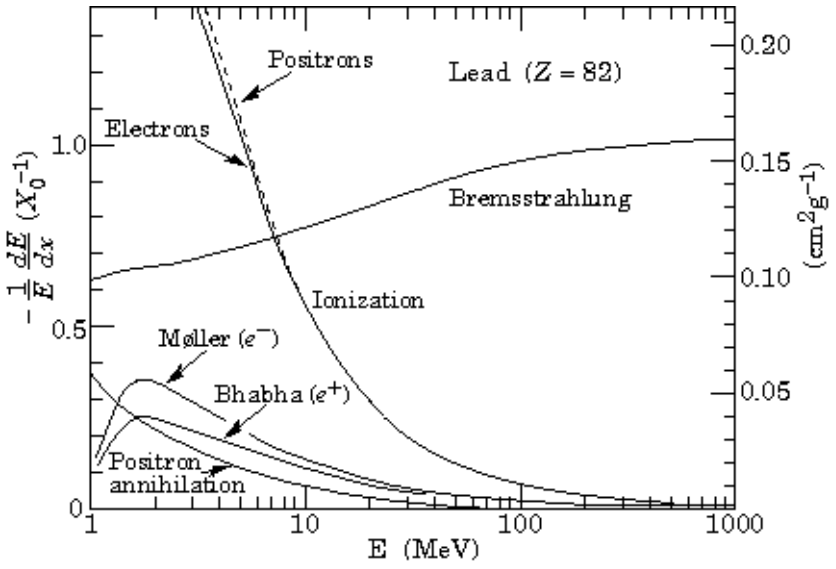


Figure 1.1: Fractional energy loss per radiation length in lead as a function of electron or positron energy [2].

they primarily lose energy via ionization. Ionization loss by electrons and positrons differs from loss by heavy charged particles mainly because of two things:

- **Their small mass:** Can not assume the incoming particle remains undeflected during the collision process.
- **Identical Particles:** For electrons, the collision are between identical particles, so it has to be taken into account the indistinguishability of the incoming electron and the electrons which it collides with.

When this is taken into account, the Bethe-Bloch formula needs some modification. In particular, the maximum energy transfer becomes $W_{max} = T_e/2$ where $T_e$ is the kinetic energy of the incident electron or positron. The Bethe-Bloch formula then becomes [1]

$$-\frac{dE}{dx} = 2\pi N_A r_e^2 m_e c^2 \rho \frac{Z}{A}\frac{1}{\beta^2}\left[ ln\frac{\tau^2(\tau+2)}{2(I/m_e c^2)^2} + F(\tau) - \delta - 2\frac{C}{Z}\right], \quad (1.3)$$

where $\tau$ is the kinetic energy of the particle in units of $m_e c^2$. $F(\tau)$ is a function which depends on whether the incoming particle is a positron or an electron.

High energy electrons, due to their low mass, can also lose energy via the process referred to as *bremsstrahlung*. The electrons will here radiate photons while being decelerated in the Coulomb field of a nucleus. The

average energy loss, dE, caused by bremsstrahlung per unit path length, dx, is given by [3]

$$-\left(\frac{dE}{dx}\right)_{Brem} = 4\alpha N_A \frac{Z^2}{A} r_e^2 E \ln\frac{183}{Z^{1/3}} = \frac{E}{X_0} \ . \tag{1.4}$$

where $X_0$ is the radiation length. Comparing Eq 1.3 and Eq 1.4 shows that the ionization loss varies logarithmically with energy while bremsstrahlung losses rise nearly linearly with E [1, 2]. This is also seen in Fig 1.2.

For high energies where collision loss can be ignored relative to radiation loss, the energy loss is given by the radiation length:

$$\frac{dE}{dx} = -\frac{E}{X_0} \ . \tag{1.5}$$

Integrating this yields:

$$E = E_0 e^{-X/X_0} \ . \tag{1.6}$$

This means the radiation length represent the mean distance an electron or a positron travels before it has reduced its initial energy by a factor e due to bremsstrahlung. The radiation length is a function of the material properties given by [2]

$$X_0 = \frac{716.4 \text{ g/cm}^{-2} \ A}{Z(Z+1)\ln(287/\sqrt{Z})} \ . \tag{1.7}$$

The energy loss by radiation depends strongly on the absorbing material. For each material one can define a *critical energy*, $E_c$, defined as where the radiation loss is equal to the collision loss [1]

$$\left(\frac{dE}{dx}\right)_{rad} = \left(\frac{dE}{dx}\right)_{coll} \quad \text{for E} = \text{E}_C \ . \tag{1.8}$$

Loss due to bremsstrahlung will dominate above this energy. An approximate value for the critical energy is given by

$$E_c \simeq \frac{800MeV}{Z+1.2} \ . \tag{1.9}$$

## 1.2 Photon Interaction with Matter

When a beam of photons with intensity $I_0$ traverses a material of thickness x, it will be attenuated:

$$I(x) = I_0 e^{-\mu x} \ , \tag{1.10}$$

$\mu$ is the linear absorption coefficient.

Photons will interact with matter in different ways, depending on the energy of the photon and the matter they travel through. The main three interaction mechanisms will be explained in the following.

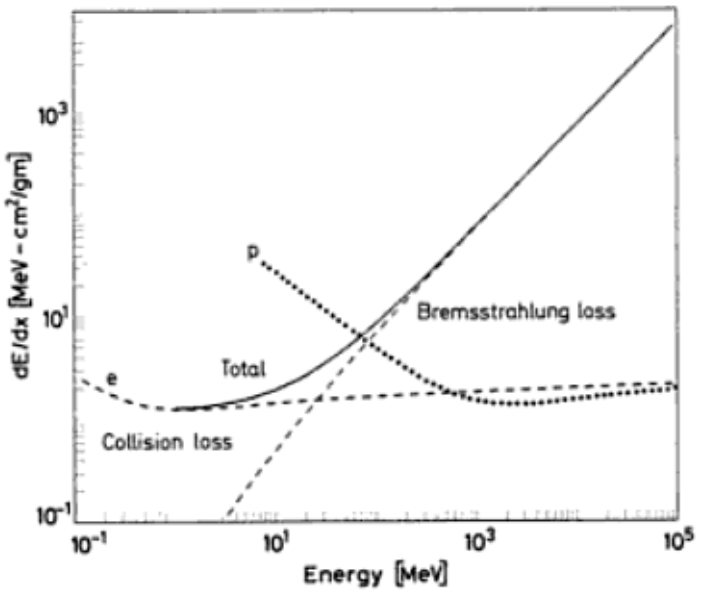


Figure 1.2: Radiation loss vs collision loss for electrons in copper. For comparison, the dE/dx is shown for protons [1].

### 1.2.1 Photoelectric effect

If a photon interacts with and transfer all of its energy to an atomic electron, it is called the *photoelectric effect*. This will lead to an ejection of a *photoelectron*, and the kinetic energy of the electron will be [4]:

$$E_e = E_\gamma - E_b \ . \tag{1.11}$$

$E_b$ is the binding energy of the electron and $E_\gamma$ is the energy of the photon.

Due to conservation of momentum, this happens preferably for bound electrons in shells near the nucleus. Also, this effect will be more important for heavy atoms and lower photon energies, as can be seen from the formula for the photoelectric cross section [3]

$$\sigma_{ph} = K\frac{Z^5}{\epsilon^{7/2}} \ , \tag{1.12}$$

where K is a constant while $\epsilon = E\gamma/(m_e c^2)$.

### 1.2.2 Compton Scattering

In compton scattering a photon interacts with a free or a weakly bound electron ($E_\gamma >> E_b$) and transfers part of its energy to the electron. This is the case for the outer, least tightly bound electrons in the scattering atom. Conservation of energy and momentum allows only a partial energy transfer

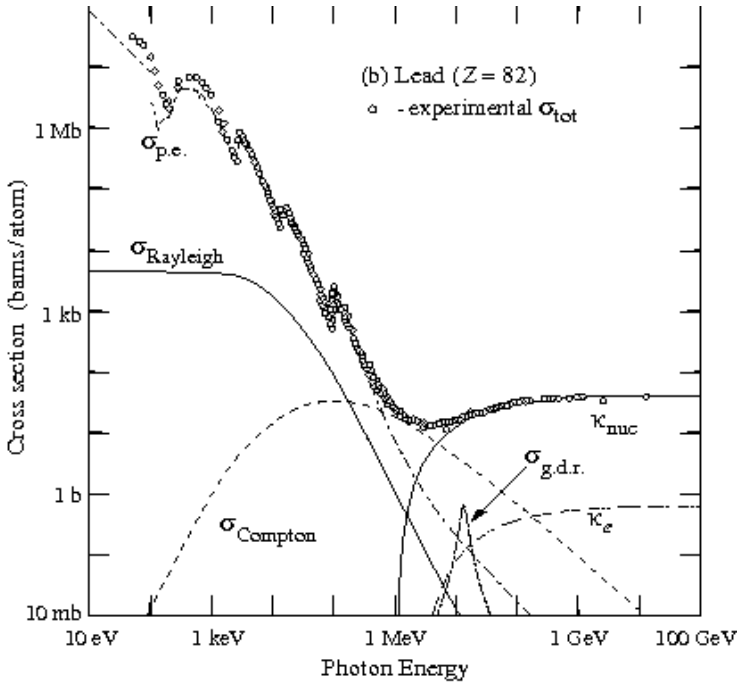


Figure 1.3: Photon total cross section as a function of energy in lead. $\sigma_{p.e}$ = Photoelectric effect, $\sigma_{Rayleigh}$ = Rayleigh scattering, $\sigma_{Compton}$ = Compton scattering, $\kappa_{nuc}$ = Pair production nuclear field, $\kappa_e$ = Pair Production, electron field, $\sigma_{g.d.r}$ = Photonuclear interactions (giant dipole resonance) [2].

when the electron is not bound tightly enough for the atom to absorb recoil energy [5]. The energy of the photon after the interaction can be calculated by the following formula [6]:

$$E'_\gamma = \frac{E_\gamma}{1 + \frac{E_\gamma}{m_e c^2}(1 - \cos(\theta_c))} \quad , \tag{1.13}$$

where $\theta_c$ is the angle between the incoming and scattered photon. $E_\gamma$ and $E'_\gamma$ is the energy of the incoming and the scattered photon, $m_e c^2$ is the rest energy of the electron = 511 keV.

The cross section for Compton scattering per atom in the absorber depends on the number of electrons available as scattering targets, and therefore increases linearly with Z [4].

### 1.2.3 Pair Production

The photon can convert into a positron-electron pair if the photon energy is greater than $2m_e c^2 = 1.022$ MeV and in addition is in the vicinity of a

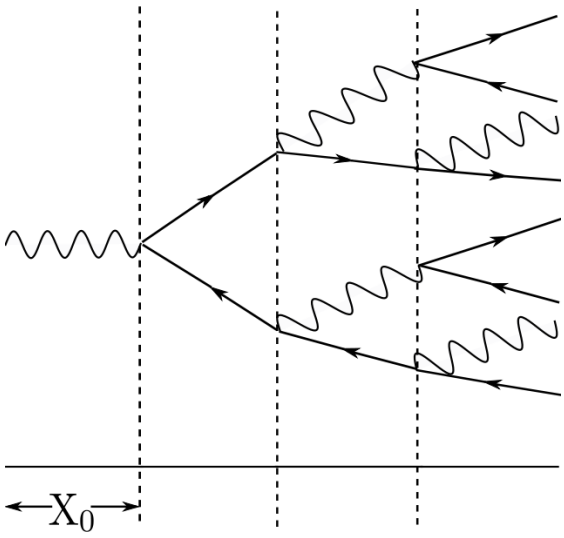


Figure 1.4: A schematic view of the electromagnetic cascade. A highly energetic photon will on average after one radiation length $X_0$ convert into a $e^+e^-$ pair. This $e^+e^-$ pair will then emit bremsstrahlung photons eventually causing a cascade of photons, electrons and positrons.

nucleus. This process is referred to as *pair production*. The cross section increases for higher photon energies above the pair production threshold. An important parameter is the radiation length, here defined as 7/9 of the mean free path, $\lambda_{pair}$, for pair production by a high-energy photon:

$$X_0 = \frac{7}{9}\lambda_{pair} \quad . \tag{1.14}$$

Fig 1.3 show the different contributions to the photon cross section in lead. At low energies it is seen that the photoelectric effect dominates, although photonuclear absorption, Compton and Rayleigh scattering also contribute. The photoelectric cross section is characterized by discontinuities in the curve, or absorption edges, which correspond to the binding energies of electrons in the various shells of the absorber atom [2].

## 1.3 Electromagnetic cascades

Using the combined effect of pair production by high energy photons and bremsstrahlung emission by electrons and positrons, this simplified view of an electromagnetic shower can be described:

1. A high energy photon with energy $E_0$ will convert into a $e^+e^-$ pair with a probability of 7/9 after traversing one radiation length $X_0$ of the material. The $e^+$ and $e^-$ have on average an energy $E_0/2$ each.

2. After on average one $X_0$, the $e^+e^-$ pair will lose energy by emitting energetic bremsstrahlung photons with approximately half the energy of the charged particle.

3. The bremsstrahlung photons will in turn create new $e^+e^-$ pairs.

4. This process will continue until the energy of the $e^+$ and $e^-$ fall below the critical energy, see Eq 1.9. At this point the $e^+$ and $e^-$ lose their energy preferably via atomic collisions rather than bremsstrahlung emission.

The total number of particles (electrons, positrons and photons) at the end of n radiation lengths will be [3]

$$N \simeq 2^n \quad . \tag{1.15}$$

The maximum penetration depth $n_{max}$ of the cascade can be found by assuming that the shower stops abruptly at the critical energy [1]. This $n_{max}$ is given by

$$n_{\max} = \frac{\ln \frac{E_0}{E_c}}{\ln 2} \quad . \tag{1.16}$$

The maximum number of particles produced is then

$$N_{\max} \simeq \frac{E_0}{E_c} \quad . \tag{1.17}$$

This shows that the maximum number of particles is proportional to the initial energy of the particle entering the material.

The transverse development of an electromagnetic shower in different materials is most conveniently measured in terms of the Moliere radius, $R_M$, given by

$$R_M = X_0 \, E_s/E_c \quad . \tag{1.18}$$

where $E_s \approx 21$ MeV [3]. More than 90% of the energy lies inside the cylinder with radius $R_M$ and about 95% is contained inside of $2R_M$. In order to decrease the transversal extension of the shower, the Moliere radius should be small.

## 1.4 Hadronic cascades

The energy measurement of hadronic cascades are similar to that of the electromagnetic ones. A high energy hadron, for instance a pion, can interact strongly with the nucleons in the material when traversing a block of matter. The strong interaction is more complex than the electromagnetic one, which makes a detailed understanding of the hadronic cascades complicated. The process is still the same, secondary hadrons will be produced when the

hadron interacts with the material. These secondary hadrons can in turn interact with the material, producing more hadrons. When the hadron energies are so small that they are stopped by ionization energy loss or absorbed in a nuclear process, the cascade ends.

Some of the hadronic particles also have electric charge, and will produce showers that are partially electromagnetic.

To describe the spatial development of the hadronic cascade the nuclear absorption length $\lambda$ is introduced. It is given by the equation [3]

$$\lambda = \frac{A}{\sigma_i N_A \rho} \quad . \tag{1.19}$$

Here A is the mass of one mole of material, $\sigma_i$ is the cross-section for inelastic scattering. Typical values for $\lambda$ is 17.1 cm for iron, 18.5 cm for lead and 12.0 cm for uranium [3].

## 1.5 Scintillators

### 1.5.1 Inorganic Scintillators

Inorganic crystals are scintillating materials which have high densities (usually $\sim$ 4-8 g/cm$^3$). In addition, they have a high effective atomic number. This makes them suitable in applications where high stopping power or a high conversion efficiency for electrons and photons is required [7]. An example of this is a total absorption electromagnetic calorimeter, see section 3.1. In addition, many of the inorganic crystals have very high light output. This will provide excellent energy resolution, even for low energies ($\sim$ few hundred keV).

The scintillation mechanism in inorganic materials depend on the energy states determined by the crystal lattice of the material [4]. For more details on the energy band structure, see section 2.2. If a photon is absorbed, this could lead to the excitation of an electron from the valence band to the conduction band, leaving behind a hole in the normally filled valence band. The electron will de-excite and a photon will be emitted. Normally the forbidden energy gap is of such a size that the emitted photon are in the ultraviolet range.

By adding small amounts of an impurity, also called activators, energy states within the forbidden energy gap are created. The energy states are referred to as recombination centers, or *luminescence centers*, and their energy structure determines the emission spectra of the scintillator. Examples of activators are thallium (TI) or cerium (Ce). Fig 1.5 shows the energy levels of an inorganic crystal where an impurity has been added.

A particle traversing the crystal will form a large number of electron-hole pairs. These e-h pairs will drift through the lattice until they encounter an activator, which they transform into an excited state. When the excited

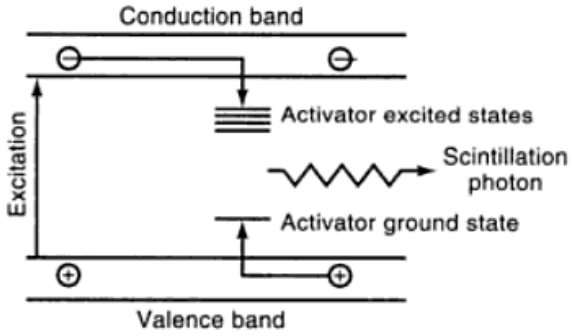


Figure 1.5: Energy band structure of an activated crystalline scintillator [8].

| | $Z_{eff}$ | Density [g/cm$^3$] | $X_0$ cm | $\lambda$ [nm] | $\tau$ [ns] | Light yield [photons/MeV] |
|---|---|---|---|---|---|---|
| NaI(TI) | 32 | 3.67 | 2.59 | 415 | 230 | 38000 |
| CsI(TI) | 54 | 4.51 | 1.86 | 540 | 680, 3340 | 65000 |
| BGO | 19 | 7.13 | 1.12 | 480 | 300 | 8200 |
| $BaF_2$ | 52 | 4.89 | 2.03 | 220 | 0.6 | 2000 |
| LSO | 65 | 7.40 | 1.14 | 420 | 47 | 25000 |
| $PbWO_4$ | 31 | 8.28 | 0.89 | 420-500 | 5, 15 | 100 |

Table 1.1: Characteristics of different inorganic scintillators. $Z_{eff}$ if the effective atomic number, $X_0$ is the radiation length, $\lambda$ is the wavelength of the emitted spectra and $\tau$ is the decay time of the scintillator [6, 4].

state decay back to the ground state, a photon is emitted. If the activator is properly chosen, this transition can now give rise to a visible photon, as the energy of this process is less than that of the full energy gap. The de-excitation will occur with half-lifes in the order of 50-500 ns, depending on the excited state in question [3, 4]. Also, keeping the amount of activators low minimizes the self-absorption of the scintillation process.

A pulse height spectrum of $^{137}$Cs, where $E_\gamma = 0.662$ MeV, is shown in Fig 1.6. As can be seen, the spectrum is separated into two parts, the first is the Compton continuum arising from the continuous energy transfer to the electron via Compton scattering. The second is the photopeak, where the photon has lost all of its energy to the electron at once via the photoelectric effect. Ideally this peak would appear as a sharp, narrow line, but due to finite energy resolution of the detector, the photopeak will have a finite width, also referred to as the Full Width of Half Maximum (FWHM). If the

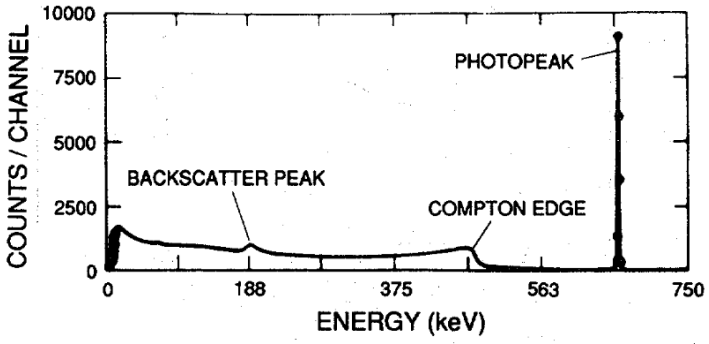


Figure 1.6: Pulse height spectrum of $^{137}$Cs showing full-energy photopeak, Compton edge and backscatter peak from the 662 keV gamma ray. Events below the photopeak are caused by Compton scattering in the detector and surrounding material [5].

photopeak is assumed to have a Gaussian shape, the FWHM is

$$FWHM = \frac{2.35}{\sqrt{N}} \ , \tag{1.20}$$

where N is the mean number of photoelectrons produced. As N increases, the FWHM will decrease and hence an improvement of the energy resolution, see below. This makes crystal which have high light yield, such as LSO, very interesting for detection of low energy particles. This is the case in PET-detection, see section 3.2.

If it is assumed that the statistical broadening of the peak is the predominate source of resolution loss, the variation of the resolution with gamma-ray energy can be predicted by noting that the FWHM of the peak is proportional to the square root of the gamma-ray energy. The produced average pulse height is directly proportional to the gamma-ray energy. The energy resolution R is given as the ratio of FWHM to the mean pulse height of the photopeak $H_0$ [4]:

$$R \equiv \frac{FWHM}{H_0} = K\frac{\sqrt{E}}{E} = \frac{K}{\sqrt{E}} \ , \tag{1.21}$$

where K is a constant of proportionality. However, the measured energy resolution as a function of energy deviates a bit from the predicted linearity, especially for low energies. This is due to imperfections and inhomogeneities of the crystal.

### 1.5.2 Organic Scintillators

The fluorescence process in organics is not based on the crystal lattice structure seen in inorganic scintillators, but arises from transitions made

by free valence electrons of the molecules. Here it is the molecular levels of a primary fluorescent material that are excited, and during de-excitation photons will be emitted in the ultraviolet range. However, this light is usually absorbed by the material due to the short absorption length, which is in the orders of a few millimeters [3, 9]. In order to extract the light, a fluorescent agent is introduced acting as a wavelength shifter. The ultraviolet light is converted into visible light. The fluorescence agent is chosen such that its absorption spectra matches that of the emission spectra of the primary component [3]. The emission spectra of the agent should in addition match the spectral dependence of the subsequent photodetector. If this is not the case, a second agent are sometimes added [9].

Of all organic detectors in nuclear and particle physics, plastic scintillators are probably the most widely used. They offer a fast signal in the order of 2-3 nanoseconds [1], which is better than most inorganic scintillators. The light yield is, however, not as high as for some of the inorganic ones. They are also quite flexible and can be made in any desirable form and they are relative inexpensive. Therefore, plastic scintillators are frequently used in large calorimetric detectors [3].

# Chapter 2

# Photodetectors

Photon counting and time-correlated photon counting techniques have been developed over many years by using the PhotoMultiplier Tubes (PMTs). Recently special semiconductor detectors have been developed, the Multipixel Avalanche Photodiode (MAPD). These devices can compete with the PMTs with respect to high gain, single photon counting and timing resolution. In addition, they are insensitive to magnetic field, which facilitates new applications unsuitable for PMTs.

In this chapter different photodetectors will be discussed, with special focus on MAPDs and how they work.

## 2.1 Photomultiplier Tube

The PMT was developed in the 1930's, and is still a very commonly used photodetector. The high gain, low noise, high frequency response and large area of collection makes it a valuable detector with many applications.

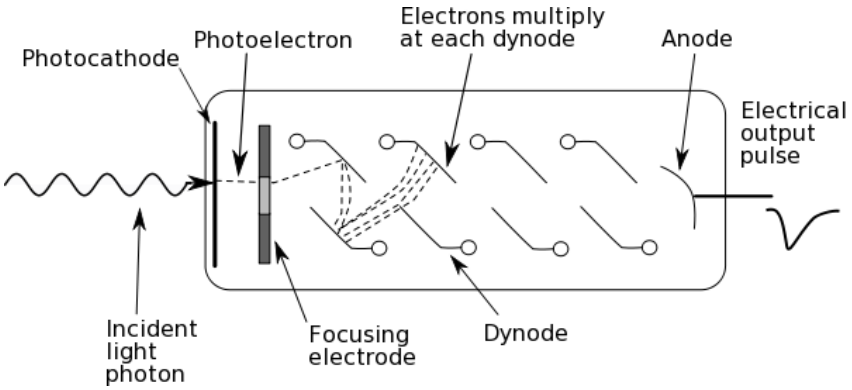


Figure 2.1: A schematic view of a photomultiplier tube, indicating an increase in electron current between successive dynodes.

In the PMT, when an incoming photon hits the photocathode, it is converted into a photoelectron (pe) via the photoelectric effect, Fig 2.1. The photoelectron is then accelerated and guided by electric fields to the first dynode, where it knocks out several electrons ($\geq$3). These secondary electrons are accelerated towards the next dynode where they release more electrons. This will create an avalanche of electrons, which are collected at the anode for delivery to the external curcuit.

The amplification factor, or gain, of a PMT depends on the number of dynodes and the applied high voltage V as $G = AV^{kn}$. n is the number of dynodes and A is a constant. k depends on the dynode material and is typically $\sim$ 0.7-0.8. G is typically in the range $10^5$- $10^6$. Pulse risetime are usually in the few ns range [1, 7].

The disadvantage of PMTs are that most of them are bulky, vulnerable to magnetic field and if a high quantum efficiency and a fast response is required, they are relative expensive. The quantum efficiency of a typical PMT is 20-30% [4].

## 2.2 Semiconductors

Semiconductors are crystalline materials whose outer shell atomic levels exhibit an energy band structure [1]. Fig 2.2 shows a simplified representation of the band structures for semiconductors, conductors (metals) and insulators.

The highest energy band is the *conduction band* and represents those eletrons that have sufficient energy to be free to migrate through the crystal. The lowest energy band is called the *valence band* and represent those electrons that are more bound to their respective atoms, they are essentially bound at lattice sites. The gap in between is called the *forbidden energy gap*, where there are no available energy levels.

The band structure determines if the material is an insulator, a conductor or a semiconductor. Metals do not exhibit any gap between the valence and the conduction band. Thus, electrons can easily migrate through the crystal as they only need small amounts of energy to be above the occupied states. Therefore, they have very high conductivity. At normal temperatures in an insulator, all electrons are normally in the valence band, leaving the conduction band empty. The forbidden energy gap is usually too big to excite electrons to the conduction band at thermal energies, thus the conductivity of an insulator are many magnitudes lower than for metals. The semiconductor behaves much like an insulator, but here the forbidden energy gap will be of such a size that thermal energy can excite electrons from the valence to the conduction band [1, 4].

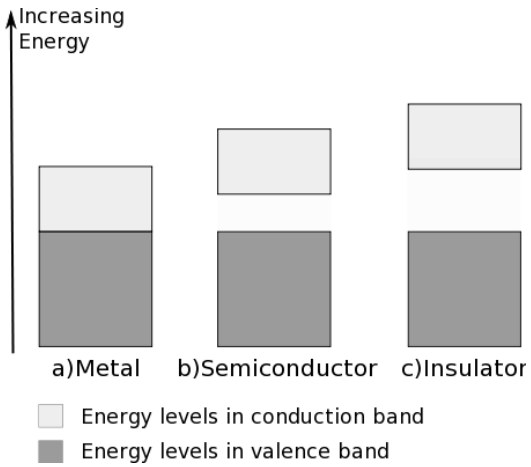


Figure 2.2: The typical energy band structure for metal, insulators and semiconductor. For semiconductors and insulators, the valence and conduction band are separated with a forbidden energy gap, where there are no available energy levels. The forbidden energy gap is smaller for semiconductors than for insulator.

### 2.2.1 p- and n-type semiconductors

In a pure semiconductor crystal, electrons occuring in the conduction band and holes in the valence band are caused by thermal excitation. The number of holes in the valence band equals the number of electrons in the conduction band. By adding a small amount of impurtiy atoms having one more or one less valence electron in their outer shell, this balance can be changed. This is also referred to as *doping*.

An example of a semiconductor is silicon (Si), which has four electrons in the valence band. In a normal crystalline structure, silicon form covalent bonds with the four nearest atoms. When adding an impurity atom having five valence electrons, which is the case for phosphorus (P), there will be one valence electron left over when all covalent bonds have been formed. This will create a discrete energy level in the forbidden energy gap, located extremely close to the conduction band, Fig 2.3a. The separation between the energy level and the conduction band is 0.05 eV in silicon and only 0.01 eV in germanium. For normal temperatures this extra electron easily gets excited to the conduction band. These doped semiconductors with electrons as mobile charge carriers are called *n-type* semiconductors [1, 4].

If the impurity atom only have three valence electrons, which is the case for aluminum (Al), there will not be enough electrons to fill the valence band. Hence, one covalent bond is left unsaturated, and a discrete energy level is created close to the valence band, Fig 2.3b. Electrons are now easily excited to this energy level, leaving extra holes behind. Such semiconductors with

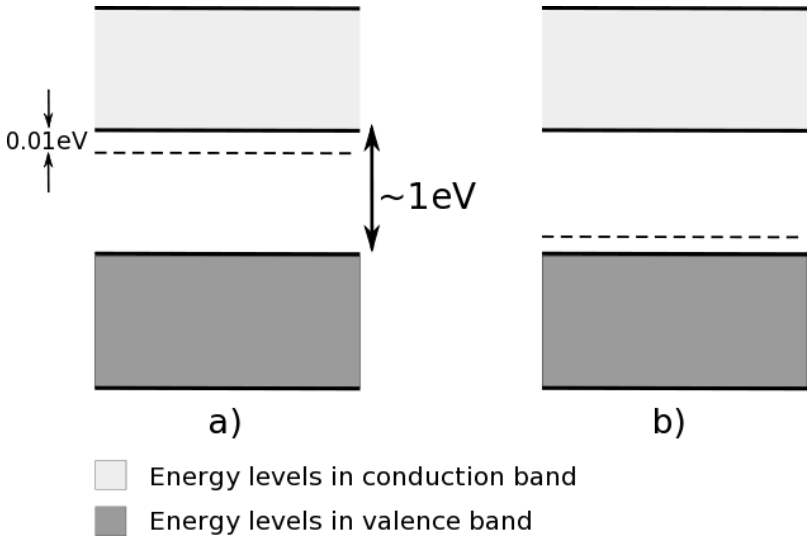


Figure 2.3: Band structure for a) donor (n-type), here a discrete energy level is created close to the conduction band, and b) acceptor (p-type), where a discrete energy level is created close to the valence band.

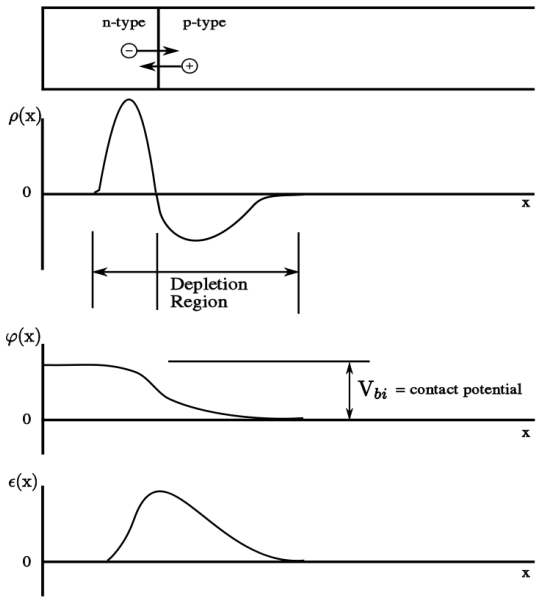


Figure 2.4: The effects of carrier diffusion across the junction give rise to the illustrated profiles for space charge $\rho$(x), electric potential $\varphi$(x) and the electric field $\epsilon$(x) [4].

holes as mobile charge carriers, are referred to as *p-type* semiconductors.

### 2.2.2 p-n junction

The pn-junction is formed by combining a p- and a n-type semiconductor in very close contact. Due to the difference in concentration of electrons and holes between the two materials, there will be an initial diffusion of holes towards the n-region and electrons towards the p-region. The n- and p-type semiconductor are initially neutral so this diffusion builds up a net negative space charge in the p-region while a positive space charge occurs in the n-region. The formation of the two adjacent space charge regions builds up a potential barrier between the n- and p-regions. The magnitude of the potential barrier depends on the doping levels. Fig 2.4 illustrate the profiles of space charge, electric potential and electric field across the junction caused by the initial carrier diffusion.

The potential barrier will eventually slow down further diffusion of charge, leaving behind a region of immobile space charge, also called the *depletion region*. Any electrons or holes entering or created in this depletion region will be swept out by the electric field, which is a very attractive characteristic for radiation detection [1].

A pn-diode with no external voltage will not perform very well. The potential created over the junction by the initial diffusion, $V_{bi}$, is of only 1 V. This is not enough to create a high enough electric field for fast carrier collection, and it also leads to a low probability for collecting the charge. In addition, the depletion region of such an unbiased junction is very small and the capacitance, see later, is very high. Therefore, the noise properties of this diode connected to the input stage of a preamplifier are quite poor [4].

If a reverse bias is applied to the junction, the situation will improve. The reverse bias voltage results in an increase in the potential across the junction, Fig 2.5. The electrons on the n-side and the holes on the p-side will be drawn away from the junction, which leads to a wider depletion region. If $N_d >> N_a$, where $N_d$ and $N_a$ is the donor and the acceptor concentration, this equation for the depletion region, $\omega_d$, can be derived [11]:

$$\omega_d = \sqrt{\frac{2\epsilon(V_b + V_{bi})}{eN_d}} \quad , \tag{2.1}$$

where $\epsilon$ the dielectric constant ($11.9\epsilon_0$ for Si). $V_b$ and $V_{bi}$ is the external and built-in voltage. One can see that higher $V_b$ gives a wider depletion region. An increased depletion region causes a greater intrinsic electric field and also a more sufficient charge collection. An another thing to note is the difference in doping concentrations. By having $N_d >> N_a$, the diode will be asymmetrically doped and the depletion region is extended predominantly into the n-side [11].

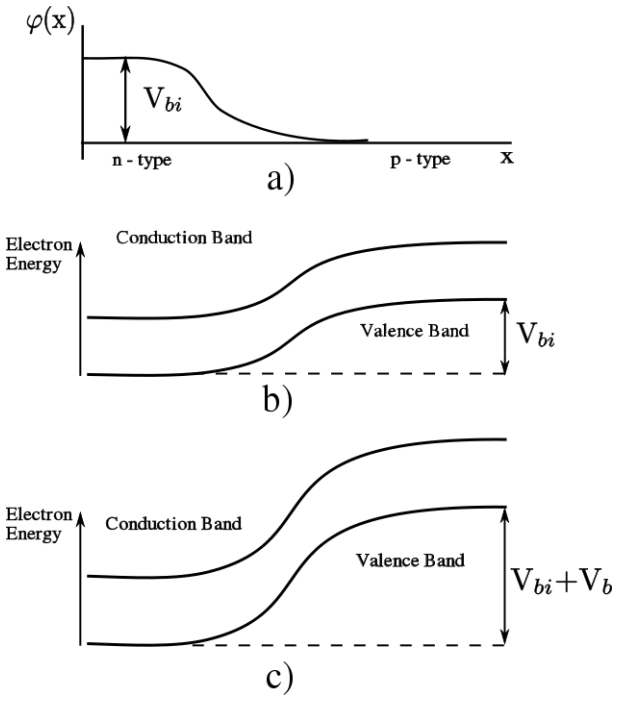


Figure 2.5: a) The variation of electric potential across an n-p junction, also shown in figure 2.4. b) The resulting variation in electron energy bands across the junction. The curvature is reversed because an increase in electron energy corresponds to a decrease in conventional electric potential $\varphi$(x) defined for a positive charge. c) The added displacement of the bands caused by application of a reverse bias voltage $V_b$ across the junction [4].

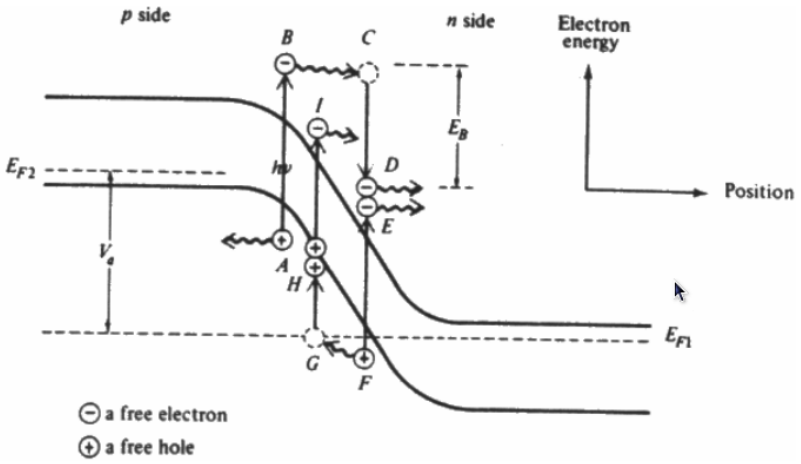


Figure 2.6: Energy-position showing the carrier multiplication following a photon absorption in a reverse-biased APD [10].

The reverse biased diode is of special interest for radiation detection. If an incident photon (in the case of Si, $E_{photon} > 1.1$ eV) is absorbed in the region where the electric field exist, it will excite electrons to the conduction band, leaving behind a hole in the valence band. If the electric field is strong enough, the field will make the electron drift to the n-side and the holes to the p-side, resulting in the flow of photocurrent in the external circuit. The time integral of this current will be one electron charge.

Because the depletion region is (ideally) a volume free of mobile carriers, it forms a capacitor with the undepleted n- and p-regions as the electrodes and the depletion region as the dielectric. The capacitance is given by [11]

$$C = \epsilon \frac{A}{\omega_d} = A\sqrt{\frac{\epsilon e N_d}{2(V_b + V_{bi})}} \quad . \tag{2.2}$$

Even in the absence of ionizing radiation, a steady leakage current is observed. This is referred to as *dark current* and occur due to thermal excitation, which promotes electrons across the bandgap [4]. Hence, the dark current is strongly temperature dependent, as can be seen from [11]

$$I_R \propto T^2 exp(-\frac{E_g}{2kT}) \quad , \tag{2.3}$$

where $E_g$ is the bandgap energy and k the Boltzmann constant. By cooling the detector, this leakage current can be reduced substantially.

## 2.3 Avalanche Photodiode

The Avalanche PhotoDiode (APD) detects light using the same principle as a p-n diode. The main difference is the operating voltage. It is high enough for the electrons, or holes, produced by photon absorption to gain enough energy to produce secondary electron-hole pairs, also called *impact ionization*. In silicon, this happens if the electric field strength is higher than $1{\cdot}10^5$ V/cm [12]. Fig 2.6 shows the carrier multiplication following the absorption of a photon. The photon is absorbed in point A, creating an electron-hole pair. The electron (B) is accelerated until point C where it has gained enough energy to create a new electron (E)-hole (F) pair. The newly generated carriers drift in turn in opposite directions. The hole (F) can also create an electron (I)-hole (H) pair, as in point G. The result of this is an avalanche of electrons and holes [10].

A competition starts between the rate at which e-h pairs are being generated by impact ionization, analogous to birth rate, and the rate at which they exit the high field region and are collected, analogous to death rate [13]. In an APD the reverse bias voltage is below the *breakdown voltage*, which causes the population of electrons and holes to decline.

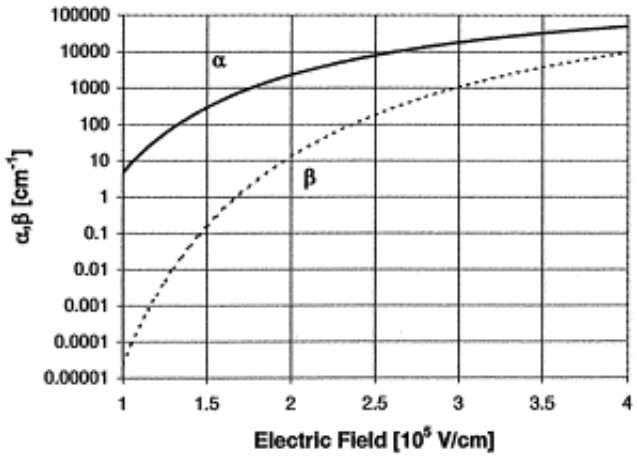


Figure 2.7: Ionization coefficients as functions of the electric field in silicon [14].

The impact ionization effect is characterized by the *ionization coefficient*, which is the average number of electron-hole pairs created by a charge carrier per unit of distance, during its transit in the high electric field [12]. For most semiconductor materials, except germanium, ionization coefficients for holes ($\beta$) and electrons ($\alpha$) differ. The ionization coefficients for electrons and holes are given by [14]

$$\alpha(E) = 2300\ exp\left[-6.78\left(\frac{2\times10^5}{E\ [V/cm]} - 1\right)\right] \quad , \tag{2.4}$$

$$\beta(E) = 13\ exp\left[-13.2\left(\frac{2\times10^5}{E\ [V/cm]} - 1\right)\right] \quad . \tag{2.5}$$

Fig 2.7 shows the ionization coefficients as a function of the electric field.

Because the ionization coefficients in silicon are much higher for electrons than for holes, the multiplication factor for electrons, $M_e$, will be higher as well. The multiplication factor as a function of the distance from the APD surface is [14]

$$M(x) = \frac{exp\left[-\int_0^x(\alpha(x')-\beta(x'))dx'\right]}{1 - \int_0^L \alpha(x')exp\left[-\int_0^{x'}(\alpha(x'')-\beta(x''))dx''\right]dx'} \quad . \tag{2.6}$$

Each absorbed photon creates on average a finite number M of electron-hole pairs, typically tens or hundred. The average photocurrent is strictly proportional to the incident optical flux, hence the term *proportional mode*. When the reverse bias voltage has exceeded the breakdown voltage, the gain,

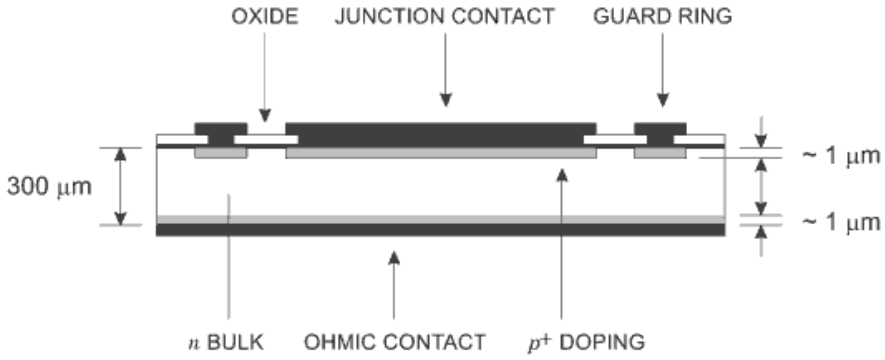


Figure 2.8: Cross section of a typical detector diode. The diode are commonly formed by introducing a highly doped surface layer into a lightly doped bulk. This ensures that the depletion region extends into the bulk [11].

at least formally, goes to infinity. This will happen in formula 2.6 when the denominator is equal to zero [13, 14].

The dependence of $\beta/\alpha$ is referred to as the k-factor. The k-factor is one of the most important APD parameters and determines its multiplication noise [14]. The gain M is the average number of electron-hole pairs created per absorbed photon, but because the impact ionization is a statistical process, the actual number varies. This fluctuation produces excess noise, or *multiplication noise*. The multiplication noise gets progressively worse with increasing reverse bias [13], and it is also material dependent. As mentioned before, electrons are much more likely to impact ionize than holes in silicon. Actually, the higher the participation the electron has on the avalanche process, the lower the multiplication noise gets [12].

Fig 2.8 shows the cross section for a typical detector diode. They are usually asymmetric, with a highly doped layer at the surface and a lightly doped bulk. With reverse bias the junction depletes into the bulk.

APDs operated close below break-down voltage, show a strong dependence of the gain on temperature and bias voltage. This leads to a requirement of very stable temperature and bias voltage. In addition, the limited internal gain of the APDs require low noise amplifiers and restricted operation bandwidth [15].

## 2.4 Multipixel Avalanche Photodiode

Limitations in gain and most of the stability problems with APDs can be avoided by setting the reverse bias voltage above the breakdown voltage [15]. This is also known as operating them in Geiger Mode. The electric

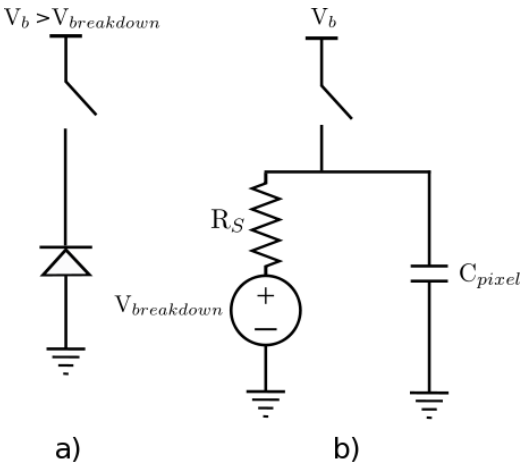


Figure 2.9: Passive quenching circuits. (a ) The APD is charged to some bias voltage above breakdown voltage and then left open circuited. (b) Subsequently, once an avalanche has been initiated, the APD behaves according to a simple circuit model [13].

field is so high that the electrons and holes multiply faster, on average, than they can be extracted. Both electrons and holes contribute to the multiplication process, causing the avalanche to diverge, and a constant current flows through the junction.

Inserting a high ohmic resistor, $R_S$, in series with the diode will make the current grow to a value limited by the resistor. More and more voltage are dropped over the resistor as the current grows, leading to a decrease in voltage over the diode. The rate of growth will slow down until the voltage over the diode is reduced to the breakdown voltage. Here the current neither grows nor decays, and the series resistor will function as a stabilizer for the current. For instance, a downward fluctuation of the current will lead to an increase of the voltage over the diode, and the current goes back up [13].

To be able to detect another photon after this, the current has to be shut off, or *quenched*. There are two ways to do this, with a *passive quenching* or a *active quenching* circuit. The active quenching circuit senses when the diode starts to discharge and then sets the bias voltage below breakdown voltage for a certain period of time until the breakdown is quenched. In a passive quenching circuit, the diode has been charged up to some bias voltage above breakdown voltage. Once an avalanche has been initiated, the diode discharges its own capacitance until it is no longer above breakdown voltage and the avalanche is quenched [13, 15].

Fig 2.9a shows a simple model of a passive-quenching circuit. The diode has been biased up to some voltage, $V_b$, above breakdown voltage, and then left opened circuted. Fig 2.9b shows the same circuit with a first

order circuit model inserted to describe the diode behavior during discharge. $C_{pixel}$ represents the capacitance of the diode. Using this as a model, one can calculate the accumulated charge, Q, in the capacitor [16]:

$$Q = C_{pixel} \cdot (V_b - V_{breakdown}) = C_{pixel} \cdot V_{over} \quad . \tag{2.7}$$

The current will decay exponentially to zero and the voltage to breakdown voltage with a time constant $R_S C_{pixel}$ [13]. The gain can now be calculated by dividing the accumulated charge with the electron charge

$$G = \frac{Q}{q_e} = \frac{C_{pixel}}{q_e} \cdot V_{over} \quad . \tag{2.8}$$

The gain depends only on the applied over-voltage $V_{over}$ and the pixel capacitance $C_{pixel}$. To reduce gain fluctuations, $C_{pixel}$ should not be too large, and the bias voltage should also be very stable. This model does not take into account the recombination of charge carriers. However, it represents a good approximation [17].

The signal out of the diode will be the same, regardless of the incoming particle, the energy of it and how many particles that hit the diode within a certain time window. This way the Geiger-mode APD performs as a digital counter, giving no information of the size of the input and thus prohibiting the possibility of having proportional information for spectroscopy. The novel photodetector Multipixel Avalanche Photodiode (MAPD)[1] overcomes this problem by having a large number of these diodes joined together on a common substrate and under a common load. Each diode is referred to as a micropixel with a typical size around 15-70 $\mu$m [18]. Each micro-pixel will produce the same, identical signal when hit, and the output of the MAPD is just the sum of all these individual signals. Thus, the MAPD as a whole, is an analogue detector that can measure the incident light intensity. By looking at the signal out, the number of pixels being struck can be extracted.

### 2.4.1 Different MAPDs

The different photodetectors are built up in different ways, leading to different characteristics, so in the following the topologies for the MAPD and the SiPM are discussed. The SiPMs are not used in this thesis, but the topology of the SiPMs are close to that of the MultiPixel Photon Counters (MPPCs).

#### MPPC/SiPM

A schematic view of a SiPM microcell and the corresponding electric field is shown in Fig 2.10. The structure of the cell consists of 4 layers, 1 n-doped

[1] There exists a lot of names on these devices, MAPD, Silicon Photomultiplier (SiPM) and MultiPixel Photon Counter (MPPC), the difference is just the manufacturer. In this thesis the name MAPD is used as a synonym of the many different types making use of basically the same principle.

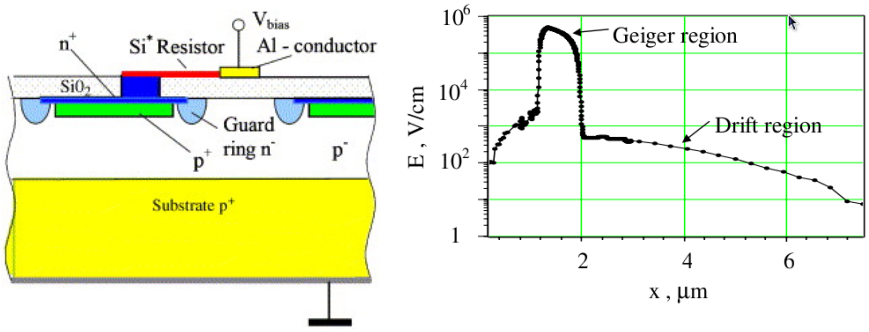


Figure 2.10: a) Schematic view of the SiPM microcell and b) Electric field distribution in epitaxy layer [18].

and 3 p-doped layers in the order $n^+$-$p^+$-$p^-$-$p^+$. The + and - indicates a high and light doping level, respectively. A few micrometer epitaxy layer on low resistive $p^+$ substrate forms the drift region with a low built-in electric field. The $n^+$ side is thin and it is this side that is illuminated through a window. A thin depletion region (0.7-0.8 $\mu$m) is created with a very high electric field (3-5 $\cdot 10^5$ V/cm) between the $p^+$ and $n^+$ layers. Here the conditions for Geiger mode discharge take place [18]. The absorption of photons, and hence the creation of an electron-hole pair, takes mainly place in the $p^-$ layer. The nearly uniform field here separates the electron and hole and drifts them at velocities near saturation towards the $n^+$ and $p^+$ sides, respectively. When the drifting electrons reach the $p^+$-layer, they experience a greater electrical field, which leads to the avalanche [19].

The resistive layer on top of the $n^+$ layer will quench the avalanche. This resistive layer on the silicon wafer can be made of various materials having a wide energy gap and suitable conductivity (for example SiC) [19]. The electrical decoupling between the adjacent pixels is provided by polysilicon resistive strips and uniformity of the electric field within the pixel by the $n^-$guard rings around each pixel [18]. All pixels are connected by common aluminum strips in order to read out the signal.

### MAPD

The topology of a MAPD is shown in Fig 2.11. It has a common p-n junction and a homogeneous entrance window as a standard APD. Both the matrix of avalanche regions and the individual quenching elements are placed inside the silicon substrate. A special distribution of the inner electric field will create individual microwells for charge trapping and collection located a few micrometers below the surface. The MAPDs can get over $10^4$ independent avalanche regions, or vertical channels, per $mm^2$, so they have a relative

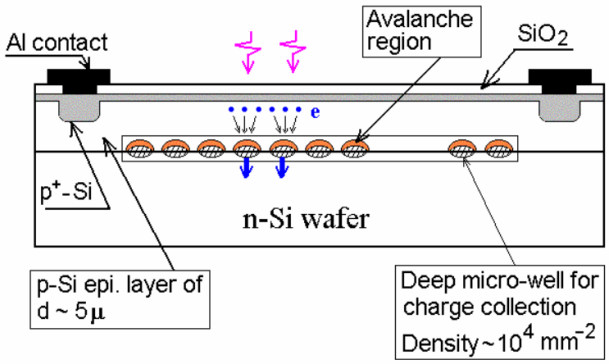


Figure 2.11: Schematic view of an MAPD with individual micro-wells [20].

| Type | Size | Pixel Density | Gain |
|---|---|---|---|
| MAPD | 3x3mm$^2$ | 10000/mm$^2$ | $< 10^5$ |
| MAPD3-A | 3x3mm$^2$ | 15000/mm$^2$ | 40000 |
| MPPC S10362-11-025C | 3x3mm$^2$ | 3600 | 2.75x10$^5$ |
| MPPC S10362-33-050C | 1x1mm$^2$ | 1600 | 7.5x10$^5$ |

Table 2.1: List of the different photodetectors used in this thesis. The MAPDs are produced by Dubna, Russia, and the MAPD3-As by Zecotek, Russia, while the MPPCs are from Hamamatsu, Japan.

high dynamical range. Charge collection in individual micro-wells provides the local self-quenching of avalanche processes in the MAPD [21]. The MAPD requires an epitaxial growing of extremely pure Si wafers and a deep ion implantation with various impurities. The quantum efficiency of these devices is reported to be 80% [20], which is considerably larger than for PMTs.

Because of the individual surface resistors, the SiPMs has a strict limit in number of pixels/mm$^2$ due to the dead areas around each individual pixel. This is avoided with the deep micro-well configuration the MAPDs are operating with, leading to a higher dynamical range. On the other hand the SiPMs and MPPCs have a higher gain than the MAPDs, making them more suitable for photon counting. Table 2.1 lists the different MAPDs and MPPCs used in this thesis. As can be seen, they vary both in gain and dynamical range. A picture of the different detectors used is shown in Fig 2.12.

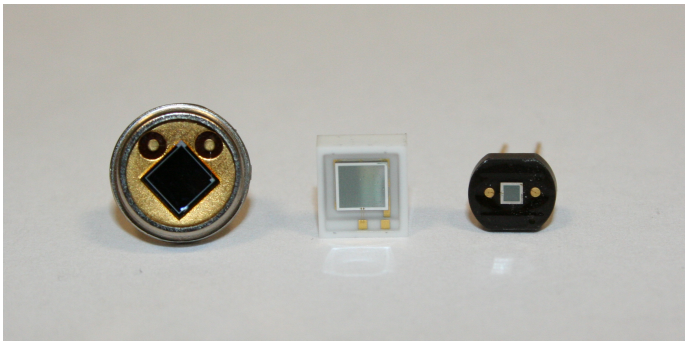

Figure 2.12: The different photodetectors. From the left: MAPD/MAPD3-A, MPPC S10362-33-050C and MPPC S10362-11-025C.

### 2.4.2 Photon Detection Efficiency

The probability that a photon will produce a detection event, are referred to as the *Photon Detection Efficiency* (PDE). The PDE is defined as [18]

$$PDE = QE \cdot \varepsilon_G \cdot \frac{A_{pixels}}{A_{total}} \tag{2.9}$$

QE is the *quantum efficiency* and is the probability that the photon is absorbed in the active region of the diode, and is highly wavelength dependent. $A_{pixels}/A_{total}$ is the effective area, or the ratio of the sensitive part $A_{pixel}$ divided by the total area $A_{total}$. For MAPDs this probability is unity [20], while for MPPCs or SiPMs the effective area is ranging from 25% to 60% [15]. $\epsilon_G$ is the probability that a single photoelectron will trigger an avalanche. $\epsilon_G$ increases with higher bias voltage, since a higher electric field will increase the probability for the primary carrier to trigger the avalanche.

### 2.4.3 Dark Rate

As mentioned in section 2.3, the gain of the APD in proportional mode has a statistical variation that leads to multiplication noise. For diodes operated in the Geiger mode, the concept of this noise does not apply. The number of electron-hole pairs is fixed by the external circuit, not by the statistics of the impact-ionization process. For example, in the simple passive-quenching case, the avalanche has no further opportunity to die out until the pixel has discharged from its initial bias voltage down to the breakdown voltage [13].

The main source for the noise in the MAPDs is the dark rate. One of the sources for the dark rate is thermally generated carriers created in the sensitive volume. These can trigger an avalanche, which is indistinguishable from a "real" one. The rate increases with temperature and reverse bias voltage.

Afterpulsing effects is another source for the dark rate. Some of the carriers may be captured by impurity levels in the depletion region during the avalanche. These are subsequently released with a delay, which depend on the impurity level actually involved, and can retrigger the avalanche. The afterpulsing effects will increase with the total number of carriers crossing the junction, or with the total charge of the avalanche pulse [22].

### 2.4.4 Dynamical Range

The dynamical range is limited due to the finite total number of pixels. For low photon fluxes this is not a problem, as the probability for two or more photons hitting the same cell is very low. For higher photon fluxes, cells have a higher probability to be hit by multiple photons at once, leading to a nonlinear response and eventually to a saturation of the output signal given by the total number of pixels. The average number of cells that will be triggered, $N_{fired}$, depends on the number of photoelectrons created, $N_{pe}$ :

$$N_{\text{fired}} = N_{\text{pixels}} \left[ 1 \; - \; e^{-\frac{N\text{pe}}{N\text{pixels}}} \right] \quad , \tag{2.10}$$

$N_{pixels}$ denotes the total number of pixels available. This approximation is only true for very fast signals, i.e. light pulses shorter than the recovery time of a pixel. For signals extended in time, late arriving photons can trigger already hit, but recovered cells [15, 23].

### 2.4.5 Thermal Effects

The breakdown voltage is strongly temperature dependent [22]. When the temperature rises, the breakdown voltage will increase as well. If the reverse bias voltage over the diode is the same, this means that the excess bias voltage, or the voltage over the breakdown voltage, will decrease. The result is a decrease in gain, as will be seen in chapter 5.

The dark rate, as mentioned, is also temperature dependent, and will decrease with decreasing temperature.

### 2.4.6 Optical Crosstalk

It is well known that during an avalanche in a reverse-biased diode, photons are emitted [24, 25]. Some of these may have enough energy to create an electron- hole pair, thus they could create an avalanche. The efficiency of photon emission has been calculated to be $\sim 3 \cdot 10^5$ photons per charge carrier crossing the junction during breakdown [24]. In the MAPDs, these photons can reach a nearby pixel where they can create an additional avalanche. This effect is referred to as *optical crosstalk* and is especially undesirable for low photon signals.

One way to limit the effect of optical crosstalk would be to lower the number of charge carriers crossing the junction, i.e. decrease the gain. This could be achieved by lowering the operating voltage. However, reducing the operating voltage will also reduce the PDE, which is not so desirable.

Another way to avoid direct crosstalk is to etch trenches between individual cells [15].

# Chapter 3

# Applications of MAPD

The advantage of being small and compact, combined with fast and insensitive to magnetic field, makes the MAPDs interesting for many applications. This chapter will focus on the use of MAPDs in calorimeters and in Positron Emission Tomography (PET).

## 3.1 Calorimeters

Calorimeters are used to measure the energy deposited by particles in the detector. There are two types of calorimeters, *electromagnetic* (EM) and *hadronic* calorimeter.

The development of an electromagnetic shower are described in section 1.3. EM calorimeters are usually used to detect light particles like photons, electrons and positrons. The best energy resolution for EM calorimeters are obtained with *total absorption homogeneous* calorimeters. Here the entire detector volume is used as an absorber and source of the detector signal. Materials with high density, e.g. inorganic scintillating crystals, are used in these calorimeters. The energy resolution can be parametrized as [7]

$$\frac{\sigma_E}{E} = \sqrt{\frac{a^2}{E} + b^2 + \left(\frac{c}{E}\right)^2} \quad , \tag{3.1}$$

where E is given in GeV. a is the stochastic term and represents statistics related fluctuations, section 1.5.1. While a is at a few percent level for a homogeneous calorimeter, it is typically 10 % for sampling calorimeters. b is the systematic, or constant term, and represent detector uniformity and calibration uncertainty. The term c is due to electronic noise.

The development of a hadronic cascade are described in section 1.4. Most large hadronic calorimeters are *sampling calorimeters*. These calorimeters have alternating layers of a passive absorber and active medium. The absorbing medium is usually a material of high density, such as lead, copper or iron [3]. The active medium may be plastic scintillators, liquid argon or

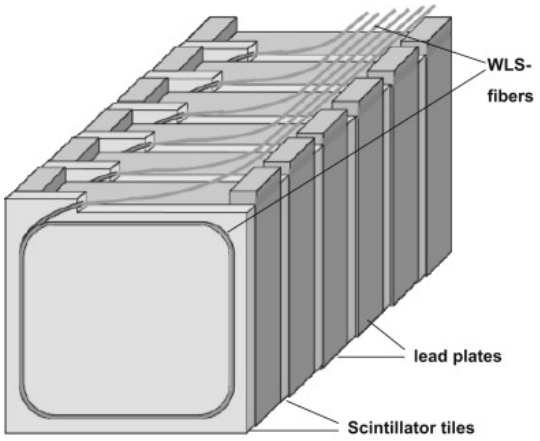


Figure 3.1: Schematic view of scintillator light readout with WLS-fibers in calorimeter module. Each module consists of 60 lead-scintillator tile [27].

gaseous detectors [7]. The ionization is measured directly or via scintillation light detected with photodetectors, such as PMTs or, as will be seen, MAPDs.

Hadron cascades in most absorbers consists of both an electromagnetic (e) component and a hadronic (h) one. The electromagnetic component rises usually from the decay of the neutral pion into two photons, $\pi^o \rightarrow \gamma\gamma$ and this is the dominant source of fluctuations in the measured energy. The effects of energy leakage, mostly caused by muons and neutrinos by pion decay which carry away energy, and the e component of the hadronic shower, leads to a energy resolution of about $\frac{\sigma}{E} \sim 0.7\text{-}0.9/\sqrt{E(GeV)}$. This holds if the thickness of material between the sampling devices is below 5 cm in iron [3].

Usually, showers induced by electrons and hadrons of the same energy do not produce the same visible energy or response, the ratio e/h is $> 1$. If this response is compensated, so that the fluctuations due to the $\pi^o$ content of the shower is reduced, and e/h = 1, the energy resolution will improve. This is done in *compensating* calorimeters, initially realized by using uranium absorbers, but have also been successfully applied to calorimeters using iron or lead absorbers [26].

## Projectile Spectator Detector

A new generation of heavy-ion experiment, for instance NA61/SHINE at CERN and Compressed Baryonic Matter (CBM) at Facility for Antiproton on Ion Research (FAIR), is focused on the search for the critical point of strongly interacting matter and analysis of deconfinement of matter [27]. This can be achieved by measuring the energy, $E_S$, carried by projectile spectator nucleons and fragments. These are non-interacting nucleons, and

their energy is the quantity most directly related to the centrality of the collision. This allows an estimate of the number of interacting projectile nucleons, $N_P$, participating in the nucleus-nucleus collision through the simple relation [26]

$$N_P = A - \frac{E_S}{E_A} \quad , \tag{3.2}$$

where A is the mass number of the projectile while $E_A$ is the beam energy per nucleon. A very forward hadron calorimeter, the Projectile Spectator Detector (PSD) has been proposed for this task. In the following, the PSD proposed for NA61/ SHINE will be discussed. The PSD will be used to measure the number of non-interacting nucleons, and this requires among other things good energy resolution, $\frac{\sigma}{E} \sim 50\%/\sqrt{E(GeV)}$ and transverse uniformity of this resolution. The design of the PSD will therefore be a full compensating lead-scintillator calorimeter, as formerly described.

**Technical Design**

The calorimeter will be located 15 meter downstream from the target, and consists of 108 individual modules arranged in a 12x9 array. Each individual module will consist of 60 lead-scintillator tile sandwiches with a sampling ratio 4:1, which means that the thickness of lead is 16 mm while the scintillator thickness is 4 mm. All 60 layers in each module will be tied together with a 0.5 mm thick steel tape and placed in a box made of the same steel before covered by another similar box. The dimension of a single module will be 10x10x160 $cm^3$ [27]. The most advanced technique for reading out light, is the use of tiles of Wave Length Shifting (WLS) fibers, which are embedded in the scintillator plates and will be employed for the PSD. This will ensure the uniformity of the light collection along the module within a few percent [26]. WLS-fibers from six consecutive scintillator tiles are collected together and viewed by a single photodetector at the end of the module [28]. Fig 3.1 shows the schematic view of one module.

Instead of the commonly used PMTs, the MAPDs are chosen to read out light due to their high gain, compactness, low cost and immunity to the nuclear counter effect, see section 2.4. The MAPDs from Dubna are used for the testing of the calorimeter, but will be changed to the improved MAPD3-As from Zecotek for the readout of the full calorimeter.

## 3.2 Positron Emission Tomography

PET is a nuclear medical imaging technique where the patient is injected with a positron-labeled radiopharmaceutical, also called a radiotracer. When injected into the patient, this radiotracer will distribute itself within the patient according to its physiologic properties where, subsequently, the radioisotope will decay and emit a positron ($\beta^+$-decay). The clinically most

| Nuclide | $E_{max}$[MeV] | $t_{1/2}$[min] | $R_{max}$[mm] | $R_{mean}$[mm] |
|---|---|---|---|---|
| $^{11}$C | 0.959 | 20.4 | 4.1 | 1.1 |
| $^{13}$N | 1.197 | 9.96 | 5.1 | 1.5 |
| $^{15}$O | 1.738 | 2.03 | 7.3 | 2.5 |
| $^{18}$F | 0.633 | 109.8 | 2.4 | 0.6 |

Table 3.1: The maximum energy $E_{max}$, half life $t_{1/2}$, and the mean, $R_{mean}$, and maximum range, $R_{mean}$, in water for the clinically most common positron emitting nuclides used in PET [6].

common radiotracer is fluor-deoxyglucose (FDG), which is $^{18}$F attached to glucose. As cancerous tissues have increased glucose metabolism, FDG is particularly suited in cancer diagnostics [6]. Other radioisotopes and some of their properties in water are shown in Tab 3.1. As can be seen, some of these nuclides have a relative short half-life, which leads to the requirement of a cyclotron nearby the scanner site. The short half-lives leads to a lower radiation dosage to patients than tracers with longer lifetimes. They are also selected due to the time scale of different human physiological processes. Examples of this is the selection of $^{15}$O as radionuclide for blood-flow measurements, while FDG is preferred in studies of slower biological processes like protein synthesis and cell proliferation [6].

The $\beta^+$-decay can happen in nuclei which have an excess of protons. The proton decays into a neutron via the weak interaction, and in the process a positron and a neutrino will be emitted. The atomic number of the daughter nucleus decreases by one:

$$ {}^{A}_{Z}X \rightarrow {}^{A}_{Z-1}Y + e^{+} + \nu \ . \tag{3.3} $$

The available energy, $E_{max}$, for the decay, also referred to as the *Q-value*, is shared between the positron and the neutrino, leading to a characteristic continuous energy spectra for the $\beta$-particles. The maximum energy that the positron can be emitted with, depends on the nuclide, and is given by the formula

$$ E_{max} = [m(^{A}X) - m(^{A}Y) - 2m_e]c^2 \ . \tag{3.4} $$

The emitted positron interacts with the surrounding tissue until it is practically at rest and finally annihilate with an electron. Two photons are created, each with an energy of 511 keV and they will be sent out back-to-back due to energy and momentum conservation. The spatial resolution of these PET detectors, usually 4-6 mm, are physically limited by the positron range, Tab 3.1, and fluctuations of emission angle between the two back-to-back photons. The latter part come from the fact that the electron and positron have some finite momentum when annihilating.

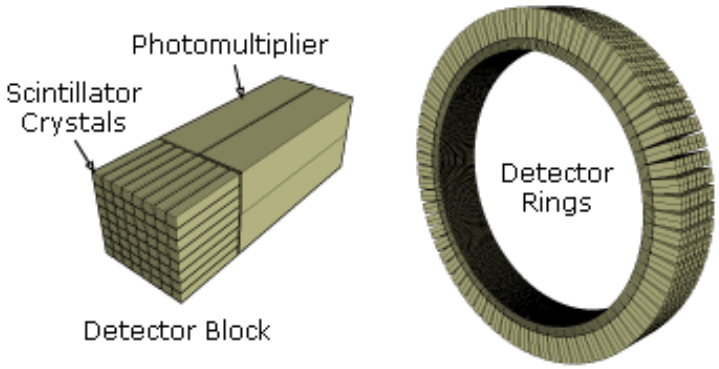


Figure 3.2: Left: One detector block consisting of scintillating crystals and photomultipliers. Right: The geometry of the detector ring.

### 3.2.1 Detection Principle in PET

The detectors form a ringlike geometry around the patient, Fig 3.2. Each detector consists of a block of scintillating crystal, in conventional PET this is usually BGO. Each block is partially sawn through to make a group of quasi-independent crystals that are optically coupled to four PMTs [29].

#### True events

Ideally, if the two photons go through the tissue without interacting with it, they will reach opposite sides of the ring. If they are detected within a certain time window, typically 10 ns, the two photons are recorded as a coincidence event, Fig 3.3a. The decay of the radionuclide is then assumed to lie on the line joining the two detector elements, also called the *Line Of Response* (LOR).

On the other hand, if the annihilated photons interact with the surrounding tissue, two false detection scenarios might happen. These processes generate noise in the clinical PET images, reducing the sensitivity of the imaging system.

#### Scattered events

In a *scattered* coincidence event, one or both of the photons interact with the tissue via Compton scattering, which makes the photons lose energy and change course, Fig 3.3b. If these photons are detected as an event, a false LOR will be computed. At 511 keV, Compton scattering is the dominant interaction process in tissue. This, together with the relative short interaction length of photons in tissue ($\sim$10 cm), lead to that only a

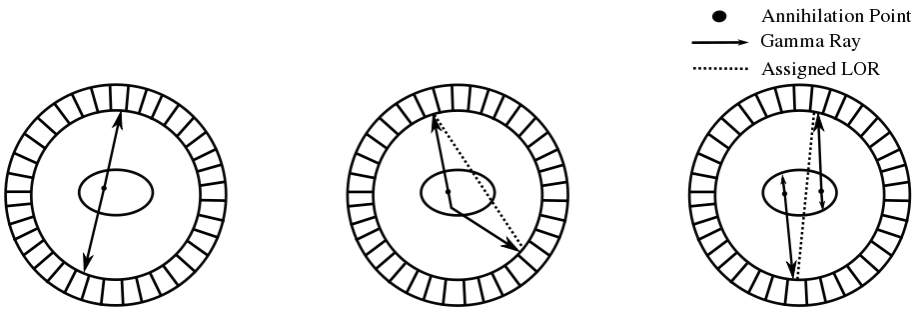


Figure 3.3: True and false events in PET. a) True event, both photons reach the detector without interacting with the surrounding tissue. b) shows that one of the photons is first scattered, then detected in coincidence, creating a false LOR. c) shows two separate events where one photon in each event interact with and loose all of its energy to the surrounding tissue. The two remaining photons are subsequently detected in coincidence.

small percentage of the annihilations will have both photons "intact" when leaving the patient [29].

To reduce the scattered events, the energy of the photons is measured. An ideal situation would thus be to accept only photons with energy of 511 keV, but because the photo peak is broaden when detected, section 1.5.1, this would lead to a huge loss of true coincidence photons. The crystal used, because of its energy resolution, will determine the size of the energy window. Better energy resolution of the crystal will lead to a more narrow energy window and hence a reduced scattered event rate [6].

### Random events

The second false event can occur if two photon pairs are created at the same time. If one photon in each pair interacts and loose all its energy to the surrounding tissue, the two remaining photons could be detected in coincidence, Fig 3.3c. This is referred to as a *random* coincidence event. The random event rate R for a given LOR which join two detector elements 1 and 2 is given by [6]

$$R = 2\tau R_1 R_2 \ , \tag{3.5}$$

where $R_1$ and $R_2$ are the single event rates for the two detector elements, and $2\tau$ is the coincidence timing window width. By reducing the timing window, the random events could be reduced. Better and faster electronics is needed for this, and hence the MAPD is a good candidate. The mean contribution to the image from random events can be measured and subtracted, but the noise resulting from the statistical variations in this rate remains [30].

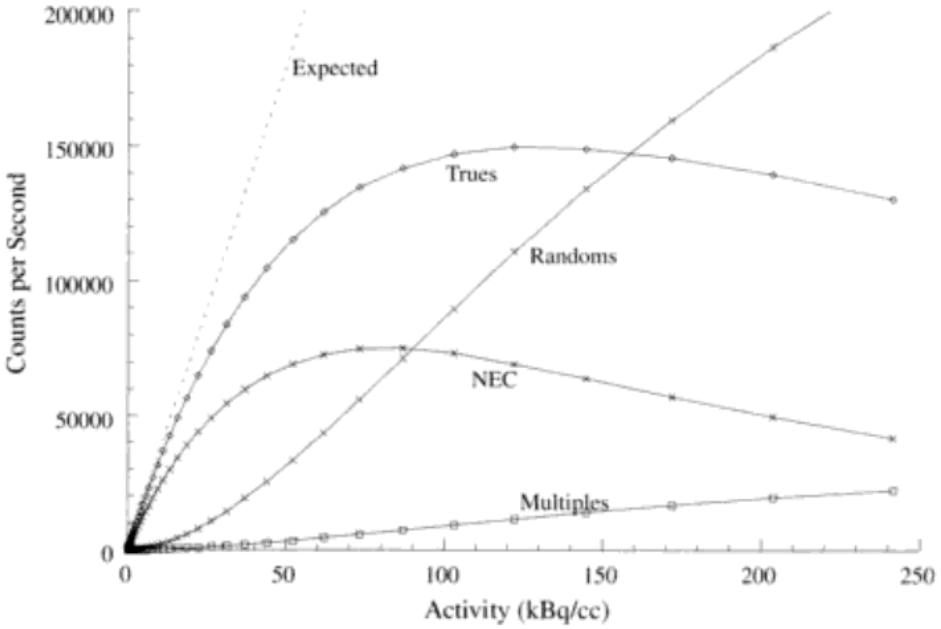


Figure 3.4: Count rate curves for the measured parameters of true (unscattered and scattered) events, random events and multiple events (three events within the same time window) and the derived curve for expected (no counting losses) and noise equivalent count rate (NECR) [6].

A common figure of merit for comparing tomographic performance, is the *Noise Equivalent Count Rate* (NECR), given by [30]

$$NECR = \frac{T^2}{T + S + 2R} \ , \tag{3.6}$$

T is the true coincidence event rate, R is the random event rate and S is the scattered event rate. The NECR is that count rate which would have resulted in the same Signal-to-Noise Ratio (SNR) in the data in the absence of scatter and random events [6]. The observed count rate is always larger than the NECR. This formalism is useful for predicting how changes in the true, scattered and random events will affect the image quality [30]. The NECR is shown, along with the data from which it was derived, in figure 3.4.

### 3.2.2 Time-of-Flight PET

In Time-of-Flight (TOF) PET detectors the difference in arrival time for the two photons is calculated and used. The principle is far from a new idea, it was proposed already in the early stages of PET scanner development. In the 1980s there were PET detectors produced using this principle using

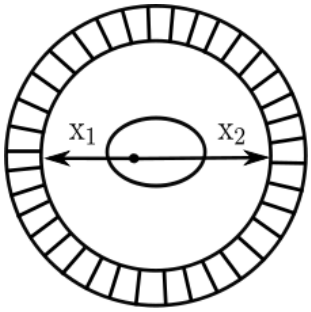


Figure 3.5: In TOF-PET the annihilation point is estimated from the difference in arrival time of the two photons. $x_1$ and $x_2$ is the distances the two photons have to travel before hitting the detector.

CsF or $BaF_2$ scintillators, but these detectors were not capable of matching neither the spatial resolution nor the sensitivity of conventional PET using BGO scintillators. By the early 1990s, these TOF scanners were retired from use.

Conventional PET image quality degrades noticeably for large patients due to increased attenuation, which leads to both the loss of true events and the increase of scattered events. The promise of TOF for clinical PET is that it has the potential to improve the image quality in heavy patients, precisely where it is needed the most [31].
Why the interest of TOF has increased, is a combination of several factors:

- The introduction of new scintillators such as LSO and LYSO. These crystals have similar high detection efficiency as BGO, but with a five times higher light output and 8 times faster decay time. This makes them also desirable for PET without TOF, so their very good timing resolution should enhance already good performance. In contrast, CsF and $BaF_2$ have very good timing resolution but their low light yield output limit the detector design choices for light sharing and decoding crystals [32, 33].

- Faster and more stable electronics, for instance the development of MAPDs

- Progress in image reconstruction algorithms

Using figure 3.5 as a model, the difference in arrival times can be calculated from

$$\Delta t = t_2 - t_1 = \frac{x_2 - x_1}{c} \quad . \tag{3.7}$$

From this the uncertainty in position can be calculated from the formula

$$\Delta x = \frac{c \cdot \Delta t}{2} \quad . \tag{3.8}$$

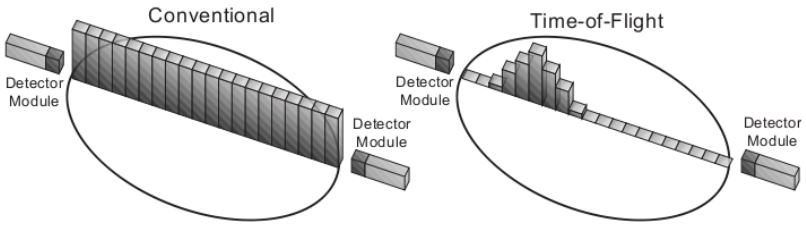


Figure 3.6: With conventional reconstruction (left), all pixels along the line are incremented by the same amount. With time-of-flight reconstruction (right) each pixel on the cord is incremented by the probability that the source is located in that pixel [30].

For instance $\Delta$t = 505 ps gives $\Delta$x = 7.56 cm. This is higher than the spatial resolution of 4-6 mm which conventional PET detectors have, so at first glance it does not seem to help. However, while constraining the annihilation position to a line segment of 7.5 cm did not improve the spatial resolution, it does reduce the statistical noise in the reconstructed image if the line segment is shorter than the size D of the patient. The multiplicative reduction factor f, corresponding to the reduction in noise variance, is given by [30]:

$$f = \frac{D}{\Delta x} = \frac{2D}{c\Delta t} \ . \tag{3.9}$$

The noise reduction is sketched in Fig 3.6. In conventional PET, each pixel along the calculated LOR is incremented by the same amount, therefore each pixel will contribute to the noise. In TOF PET each pixel is incremented with the probability that the annihilation took place in that pixel, so only the pixels nearby the pixel where the calculated annihilation took place, will contribute to the noise.

The fundamental improvement brought by TOF is an increase in SNR. The SNR improvement due to TOF reconstruction is estimated in first approximation as [34]

$$SNR_{TOF} \ \cong \ \sqrt{\frac{D}{\Delta x}}\, SNR_{conv} \ . \tag{3.10}$$

For example, for a time resolution of 300 ps, which corresponds to a position resolution of 4.5 cm, and a patient width D = 40 cm, this would yield a SNR about 3 times better than conventional PET.

# Chapter 4

# Experimental Setup

In this chapter, the experimental setups will be presented. Before going into details, a general description of the setups will be presented along with the description of the Data Acquisition (DAQ) system that has been used.

## 4.1 General Read-out Circuit

The general read-out circuit for the MAPDs is shown in Fig 4.1. The capacitor and $R_1$ will function as a low pass filter, removing high frequency noise and ripple from the power supply. This ensures a stable voltage over the MAPD. The signal out of the MAPD is a charge, which is read out as voltage over $R_2$.

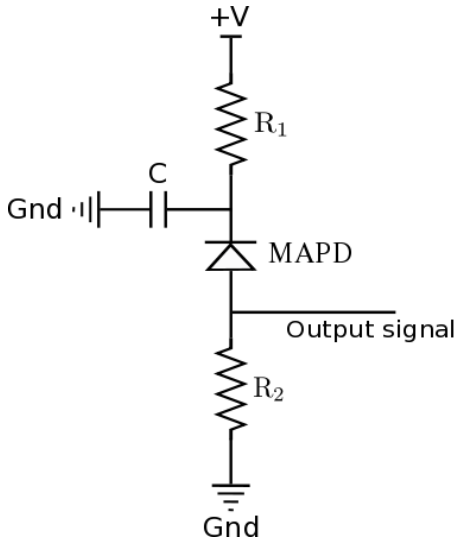


Figure 4.1: General Read-out circuit

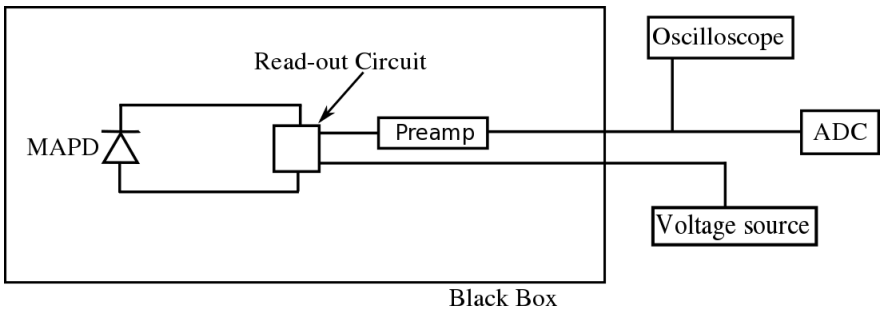


Figure 4.2: Schematic view of the prototype setup used to look at the signal from the MAPD. The voltage signal over the resistor $R_2$, Fig 4.1, is amplified with a preamplifier before directed to either the oscilloscope for visual inspection, or to the ADC. To ensure a dark environment, the MAPD has been put in a custom-made black box.

To better understand the signal, the setup shown in Fig 4.2 was used. To ensure a dark environment, the MAPD has been placed in a custom made black box. The black box are made of aluminum and the inside is covered with black filt. The voltage signal over the resistor $R_2$ is amplified with a preamplifier[1] which has a gain of 100. The impedance of this preamplifier is 50 Ω. For the experiments where the preamplifier is used, this is the same as $R_2$. The bandwidth is 100 kHz-1.5 GHz. This should ensure that the signal is not too much distorted when leaving the preamplifier. After the preamplifier, the signal is sent to either the oscilloscope[2] for visual inspection, or to the computer, as described below.

For this setup the MPPCs were used, as their gain is sufficiently high to see the dark rate. The power supply was set to the recommended reverse bias voltage given by Hamamatsu.

## 4.2 Data Acquisition System

A schematic view of the DAQ system is shown in Fig 4.3. The voltage signal over the resistor $R_2$ sent via the preamplifier, is sampled using an ADC[3]. The sampled signal from the ADC is read out using Labview, National Instruments. The software in Labview was written by Njål Brekke. The plotting has been done using ROOT [35]. A picture of the whole setup is shown in Fig 4.4.

[1] Philips Scientific Wide band Amplifier, model 6954
[2] Tektronix MSO403 Mixed Signal Oscilloscope, 350 MHz, 2.5 GS/s
[3] CAEN 4 Ch, 14 bit, 2 GHz ADC, model V1729A. Dynamical Range: -1 V to 1 V

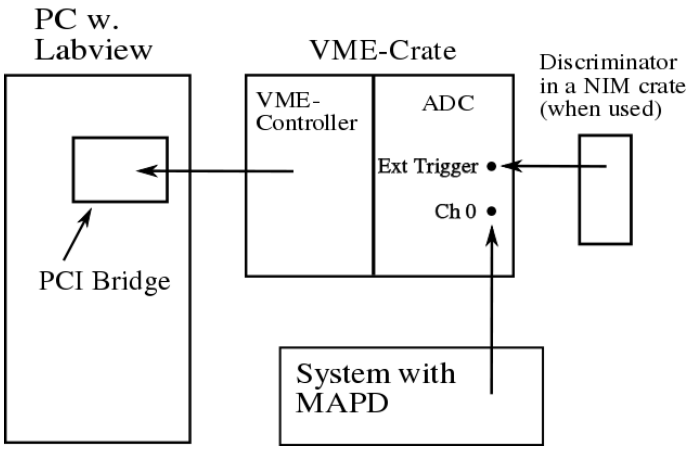


Figure 4.3: The Data Acquisition (DAQ) system used. The signal from the MAPD via the preamplifier is first sampled by the ADC, then transferred to the computer.


Figure 4.4: Picture of the setup, showing the black box, different equipment such as voltages suppliers and pulse generators, the crate with the ADC and the computer that has been used.

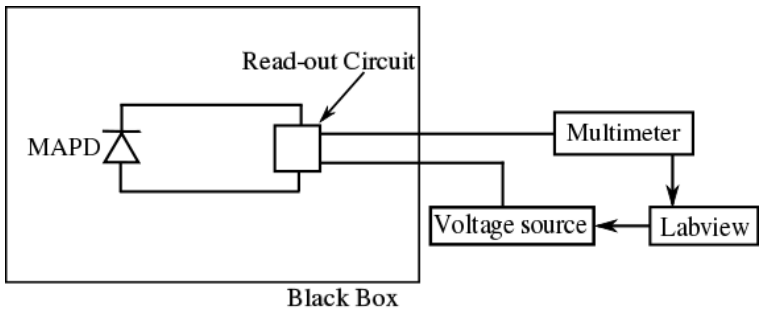


Figure 4.5: Setup for measuring the dark current. The multimeter, which reads out the dark current, and the voltage supply, which gives the voltage over the MAPD, are controlled via Labview.

### ADC

In context with these measurements, a 14-bit oversampling ADC was used, which has a dynamical range of -1 V to 1 V. The noise has been recorded for three cases:

1. Nothing was connected to the ADC.
2. The preamplifier was connected and powered up.
3. The entire system was connected to the ADC. The preamplifier was on, the MAPDs were not. The thermistor employed for the temperature measurements are also included here as they introduce noise which has to be taken into consideration.

The last part would normally have been recorded when the voltage over the detectors were on, but this has not been possible due to the very high dark rate of the MPPCs. As will be seen later, the dark rate lies in the MHz range. The noise needs also to be recorded when the voltage over the detector is on. This will mostly be done for the MAPDs and not for the MPPCs for the reason mentioned above, but this has not yet been done.

## 4.3 Dark Current

Fig 4.5 shows the setup used for measuring the dark current. The resistor $R_2$ in the read-out circuit (Fig 4.1) used in this setup was 1 k$\Omega$. Usually $R_2$ should match the input impedance on the next unit. In this setup, the next unit will be the multimeter, which has a very high input impedance, so the high $R_2$ will not be a problem. In fact, it is advantageous, since the preamplifier is not employed here. The high resistor value lead to a higher voltage signal than a low $R_2$.

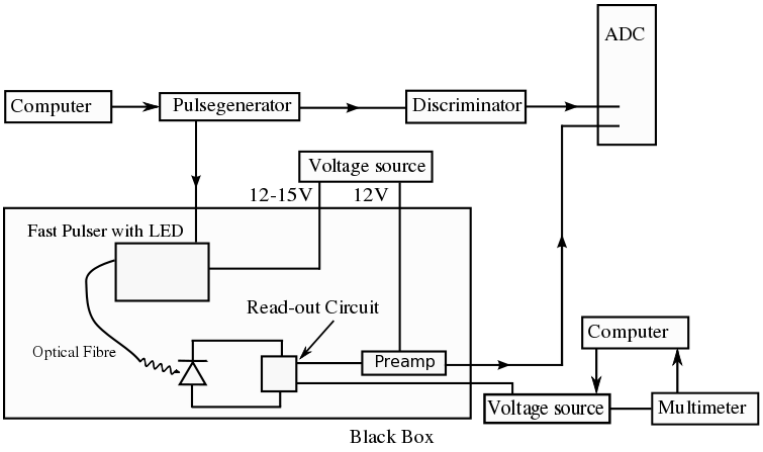


Figure 4.6: Setup for measuring the absolute gain

The multimeter [4] and the voltage supply[5] were controlled via Labview. The program in Labview did the following

1. The multimeter appeared to have an offset, so first a measurement was done to find the mean value of this offset.

2. Before running the measurements, the maximum and minimum bias voltage was set. The minimum values were usually the same for each detector type, while the maximum values were decided for each individual sample based on inspections done before each measurement to ensure that the dark current did not become too large.

3. For each bias voltage, 25 measurements of the dark current were taken and the mean + RMS-value of these were calculated. The offset value determined in step one was subtracted from the mean value.

4. Bias voltage, mean and RMS-values were stored to a textfile.

## 4.4 Absolute Gain and Dark Rate

The absolute gain and dark rate measurements were done at the same time. The resistor, $R_2$ in Fig 4.1, was in these experiments changed to 50 Ω. The setup for the absolute gain is shown in Fig 4.6. The output of the voltage source[6] was discovered to have an output voltage deviating from the value set by the user, so the actual voltages were instead determined using a multimeter. The range of voltages for each measurement was set in advance

[4]Keithley 2700 Multimeter/Data Acquisition System
[5]EA-PSI 6150-01 DC-Power Supply
[6]Keithley 487 Picoammeter/Voltage Source

by inspection. The minimum voltage was decided as the minimum voltage required to obtain a single photoelectron spectrum. The maximum voltage was either set as the highest voltage where the peaks could be separated from each other, or maximum 1.5 V over the recommended operating voltage, Appendix A.

A fast pulser has been made by Njål Brekke prior to these measurements which generated a very narrow pulse ($\sim$ 1-3 ns) with a short rise time [36]. The fast pulser requires a voltage below 23 V and the supply voltage to the pulser determines the intensity of the light pulse. An external pulsegenerator[7] creates a pulse with frequency of 2 kHz, an amplitude of 3 $V_{pp}$ and a width of 10 $\mu$s. The width of the pulse does not influence the light pulse as the fast pulser will trigger on the falling edge of the pulse.

For these measurements the fast pulser pulses the LED in such a way that only a few photons hit the MAPD. The photons are guided to the MAPD using an optical fibre. The signal from the MAPD via the preamplifier is connected to the ADC. The preamplifier is the same as mentioned in section 4.1. The pulse from the pulsegenerator is split up and guided to a discriminator[8]. This produces a fast, narrow pulse which is used as a trigger. The signal from the discriminator is then connected to the external trigger on the ADC.

For the dark rate measurements, the pulsegenerator is simply turned off.

A Labview program did the following tasks:

1. The pulse generator was turned on.

2. The voltage was set to a certain bias voltage set in advanced by the user. The real voltage value was then read out from the multimeter.

3. When the ADC was triggered by the signal from the discriminator, the sampled signal from the ADC was read from memory to Labview.

4. If photons hit the MAPD and produce a signal, the signal appears in the trigger window at the same place for each event, the time between triggering and the signal from the MAPD are constant. This way it is easy to set up a more narrow window which only include the signal. The necessary width of the window depends on the photodetector, ranging from 20-50 ns.

5. Each time the ADC was triggered by the external trigger, Labview integrated over the signal in the specified window, and also found the pulseheight. This was written to a text file for further processing.

[7] Agilent 33250A - 80 MHz Function/ Arbitrary Waveform Generator
[8] Lecroy model 620D, 8channel discriminator

6. Thermistors (temperature sensors) were attached to both the MAPD and the preamplifier, which were also connected to the computer. The temperature were read out every 10 seconds.

7. The pulse heights were plotted in a histogram, and Labview found the second peak in this histogram. This corresponds to the peak for when one photon is detected, given that no photons hit the detector in some of the events recorded. The value of the first photoelectron peak was stored for use in the dark rate measurements.

8. The pulse generator was then turned off, thus disabling the fast pulser. This ensures that the MAPD were in a completely dark environment.

9. For the dark rate an internal random trigger was used to trigger the ADC, after which a time window of 1260ns was read out.

10. A threshold was set to half of the peak height for one photoelectron found in step seven during the gain measurements.

11. If the signal exceeded this threshold value, the pulse height was found and written to a textfile.

12. The total number of triggered time windows were counted and stored.

13. Step 1) - 12) were repeated for increasing bias voltages up to a value set by the user.

During the gain measurements, it was observed that the values obtained for the gain was not stable, it tended to decrease over time. Measurements done over eight hours showed a difference of up to 8% from the first run to the last. Because the MAPDs are sensitive to temperature, a thermistor was placed close to the MAPD and also on top of the preamplifier.

To find the temperature dependence on the gain, the gain was found for a number of temperatures. For lower temperatures, the MAPD, read-out circuit and thermistor were surrounded by bottles containing ice. While the system cooled down, measurements were taken. Once the temperature had stabilized, the ice was taken away and measurements were taken while the system heated up again.

For higher temperatures, the system was instead surrounded by bottles containing hot water. The same procedure was done here, measurements were taken both when heating the system up and when it cooled down again.

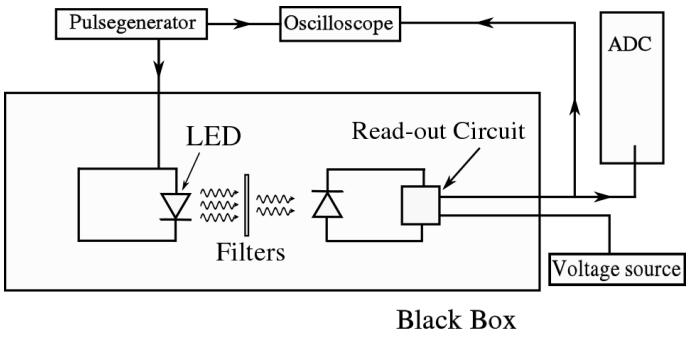


Figure 4.7: Setup for the first linearity measurement.

| Filter number | Attenuation coefficients |
|---|---|
| 0.05 | 0.912 |
| 0.2 | 0.631 |
| 0.4 | 0.398 |
| 0.6 | 0.251 |
| 0.8 | 0.158 |
| 1.0 | 0.100 |
| 2.0 | 0.010 |
| 3.0 | 0.001 |

Table 4.1: Attenuation coefficients for the neutral density filters.

## 4.5 Linearity

The setup used for the linearity measurement are shown in figure 4.7. A pulsegenerator[9] pulses the LED. The pulse has a period of 1 ms, an amplitude of 3-4 V and a width of around 20 ns. The light pulse for each measurement is fixed at either the pulse which produces the highest pulseheight in the MAPD signal, or half of this. To have a reference of the amount of light on the MAPD, neutral density filters[10] are used to attenuate the light. Table 4.1 lists the attenuation coefficients of the neutral density filters. For the first part of the linearity measurements, the voltage over the MAPD are fixed. For the second part, the same amount of light hit the photodetector while the bias voltage are changed. The signal from the MAPD are sent directly to the ADC without amplification. This is done because the largest MAPD signals produce a voltage signal that was outside the dynamical range of the preamplifier, causing the preamplifier to cut the signal.

[9]Philips PM5715 Pulse generator 1-50 MHz
[10]Newport FS-3 Absorptive ND Filter Set, 50.8x50.8 mm

## 4.6 Rise Time

The rise time of a signal is defined as the time required for a signal to change from 10% to 90% of the maximum value of the signal.

The same setup shown in Fig 4.6 has been employed here, see section 4.4 for more details. Due to the internal rise time of the preamplifier, the MAPD signal has been sent directly to the oscilloscope or ADC without amplification. The oscilloscope was used for taking pictures of the signal while the computer was used for the actual measurements.

Due to a lower SNR when doing the measurements without the preamplifier, a light pulse with high intensity was used to produce a large enough signal to measure the rise time. Labview was used to read out the signal. The program first found the highest point of the peak, and then found by interpolation when the signal crossed 10% and 90% of this value. The rise time was then easily calculated by subtracting the times at which 10% and 90% of the maximum value took place. The rise time was recorded for all samples involved in the different experiments.

# Chapter 5

# Results

In this chapter, the results obtained from the various experiments will be presented.

At first, an unexpected oscillating signal was detected, Fig 5.1a. A Fast Fourier Transformation (FFT) of the signal yielded two distinct peaks, with frequencies around 100 MHz, Fig 5.2a. The oscillating signal was seemingly unaffected of being inside or outside a shielded black box.

However, shielding the readout circuit was a solution to this problem. Thus, a new circuit board was made, this time with Surface Mounted Devices (SMDs) and then put in a box made of aluminum. This new read-out box eliminated most the unshielded wires and circuitry which could pick up noise. A picture of the two read-out circuits is shown in Fig 5.3. Looking at the signal from the new circuit showed that the oscillations had disappeared, Fig 5.1b. Applying a FFT on this signal shows that the peaks are far less distinct and the amplitudes of the peaks are much smaller, Fig 5.2b.

Later, a thermistor has been added in order to measure the temperature near the MAPDs. This unfortunately introduced some noise, the baseline was shifted to some positive value and the peak amplitudes in the FFT were increased. The thermistors had twisted pair wires, but they were not shielded. Thus, one possibility for the shifted baseline could be feedback in which the thermistors picked up signal from the output of the preamplifier. This would subsequently be picked up by the detector since the detector and the thermistor were placed very near each other, resulting in a feedback loop. The thermistor was then provided with a shielded cable, and sealed inside a copper tube welded to the copper plate, Fig 5.3, thus providing a tight electrical shield. The problem with the baseline now disappeared. The peaks in the FFT were reduced by placing the wire of the thermistor in close contactwith the shielded black box.

From these inspections it has also been seen that having the fast pulser inside the shielded black box introduce much noise. This was not seen until the end of the measurements as the frequency of this noise is higher than the

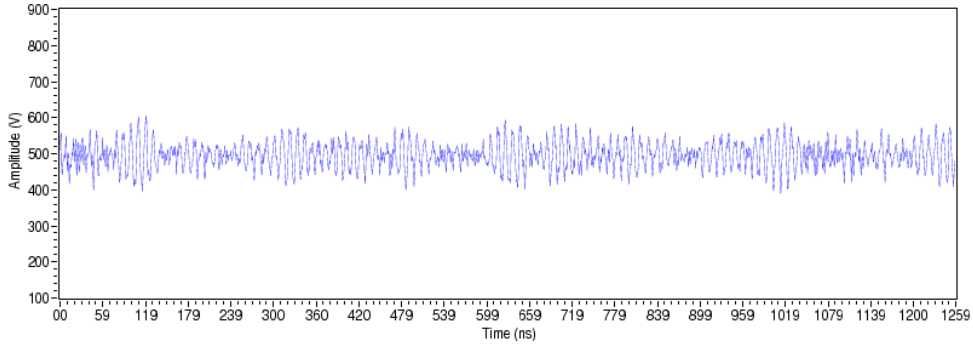


(a)

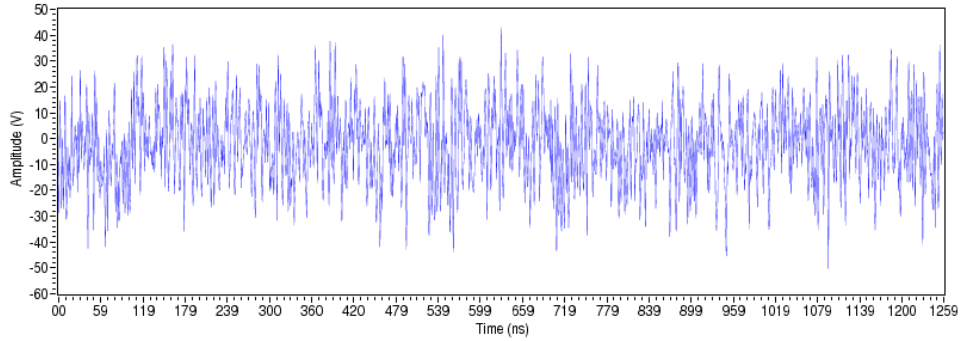


(b)

Figure 5.1: a) The signal with the first circuit showing an oscillating signal. b) Changing the read-out circuit so it is made of surface mounted devices, clearly shows that the oscillations is gone.

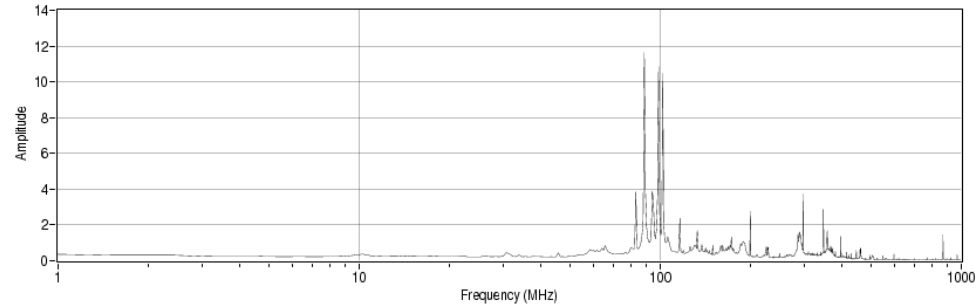


(a)

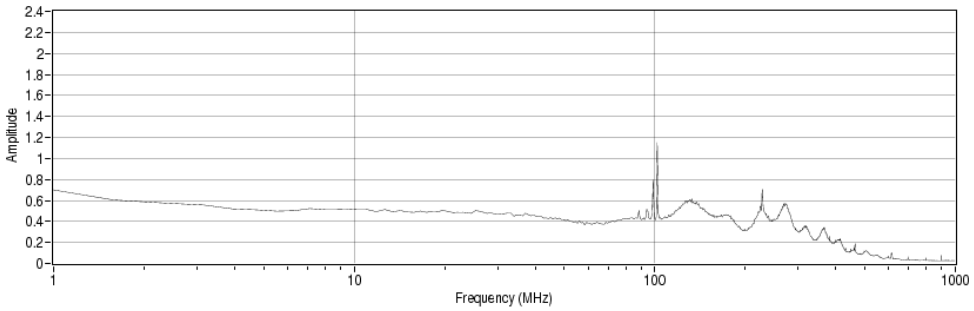


(b)

Figure 5.2: a) A Fast Fourier Transformation (FFT) of the signal shows two distinct peaks with high amplitude around 100 MHz. b) The FFT of the signal from the new read-out circuit shows that the peaks are a little less distinct, and the amplitude of the peaks are much smaller.

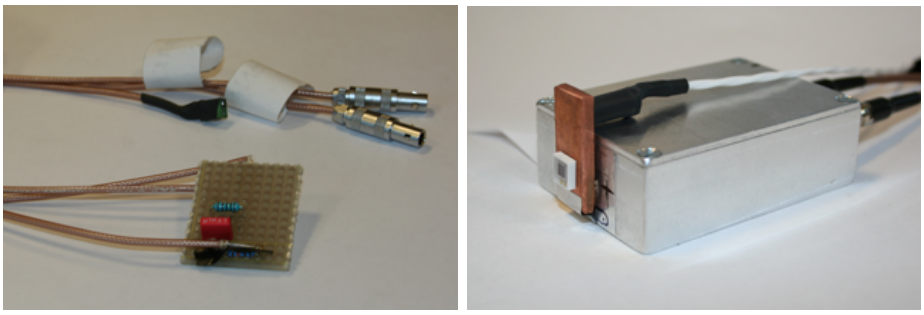

Figure 5.3: The first and second version of the read-out circuit. The second circuit is made of surface mounted devices and shielded in an aluminum box. The thermistor which measure the temperature is placed on the back of the piece of copper, which also the MAPD is placed in contact with. The new read-out circuit has a clear advantage over the first one, which has a lot of loose wires.

bandwidth of the ADC. It was first discovered when looking at the signal with an oscilloscope with a high sampling frequency[1]. Thus, it is assumed that this noise has not impacted the measurements, but should be taken into account in further experiments. It has also been noticed that the MAPDs from Zecotek and Dubna seem to be more affected by these oscillations. This is just an observation, and has to be investigated a bit more before drawing any conclusions.

## 5.1 Noise

Noise histograms for the different cases is shown in Fig 5.4. The noise for only the ADC shows an RMS value of 1.5 bins, this value puts a lower limit on measurements and will serve as a measurement error.

A summary of the RMS-values are listed in Tab 5.1. The RMS-values for the two MAPD types is seen to be a bit larger than for the MPPCs. This RMS-value is needed when setting a lower threshold to reduce the impact of the noise, usually this threshold is set to three times the RMS-value. This has not been fully done in the measurements presented here, but will be done in further experiments.

## 5.2 Dark Current

The measured signal is given in voltage V, but can easily be converted into current I by using Ohm's law:

$$I = \frac{U}{R_2} \quad . \tag{5.1}$$

As expected, the dark current is lowest for the MAPD3-As, which have the lowest gain of the 4 detector types tested.

By looking at Fig 5.5 and Fig 5.6 it can be seen that the dark current increases very rapidly for increasing bias voltage. This means that one has to be careful when setting the bias voltage, too high bias voltage will lead to a very high dark current and this will degrade the signal. If the bias voltage is sufficiently high, it can also lead to the destruction of the device. It can also be seen that there are internal differences that makes it important to characterize each of the photodetectors, this is especially the case for the MAPD3-As.

## 5.3 Absolute Gain

The integrated signal, or the charge, in ADC-counts are plotted in a histogram. Fig 5.7 shows typical single photoelectron spectrums for the two MPPC

[1]Tektronix MSO 4104 Mixed Signal Oscilloscope, 1GHz, 5GS/s

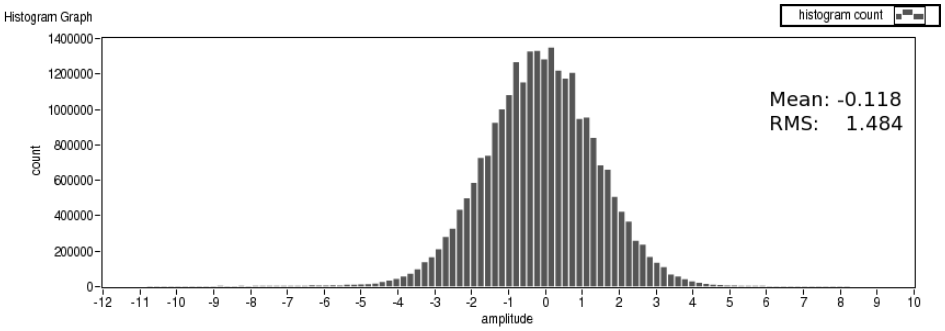


(a) The ADC with nothing connected to it

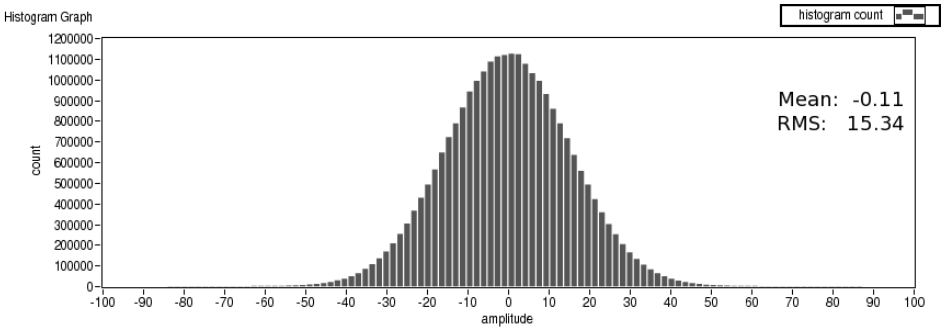


(b) The ADC with the preamplifier connected

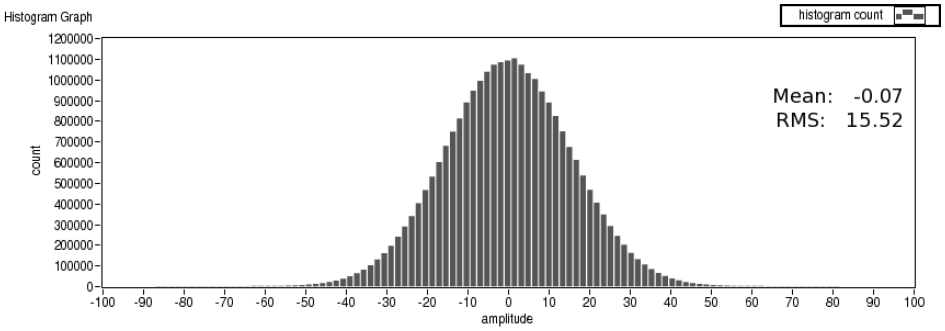


(c) The entire system is connected, here sample 341 is used as an example

Figure 5.4: Noise histograms when different components are connected to the ADC. The x-axis is given in ADC counts, the y-axis gives the intensity. The mean and RMS-value for each noise histogram is also given.

| Connected to ADC | RMS [ADC counts] | Risetime [ns] |
|---|---|---|
| Only ADC | 1.5 | |
| With preamp | 15.3 | |
| MPPC S10362-33-050C | | |
| Sample 333 | 15.8 | $2.49 \oplus 0.14$ |
| Sample 334 | 15.9 | $2.50 \oplus 0.26$ |
| Sample 335 | 15.9 | $2.49 \oplus 0.14$ |
| Sample 336 | 16.1 | $2.48 \oplus 0.14$ |
| Sample 338 | 16.0 | $2.48 \oplus 0.14$ |
| Sample 341 | 16.3 | $2.51 \oplus 0.21$ |
| MPPC S10362-11-025C | | |
| Sample 738 | 15.8 | $2.09 \oplus 0.41$ |
| Sample 739 | 15.9 | $2.06 \oplus 0.38$ |
| Sample 740 | 15.9 | $2.06 \oplus 0.31$ |
| Sample 741 | 15.8 | $2.03 \oplus 0.15$ |
| Sample 742 | 15.9 | $2.04 \oplus 0.18$ |
| MAPD | | |
| Sample 132.5 | 17.8 | $2.7 \oplus 0.6$ |
| Sample 133 | 17.6 | $2.7 \oplus 0.2$ |
| MAPD3-A | | |
| Sample 16 | 16.8 | $2.9 \oplus 0.3$ |
| Sample 23 | 16.7 | $2.9 \oplus 0.3$ |
| Sample 25 | 16.6 | $2.7 \oplus 0.2$ |
| Sample 37 | 16.8 | $2.9 \oplus 0.8$ |

Table 5.1: RMS of the noise in ADC counts. The risetime of each sample is also shown.

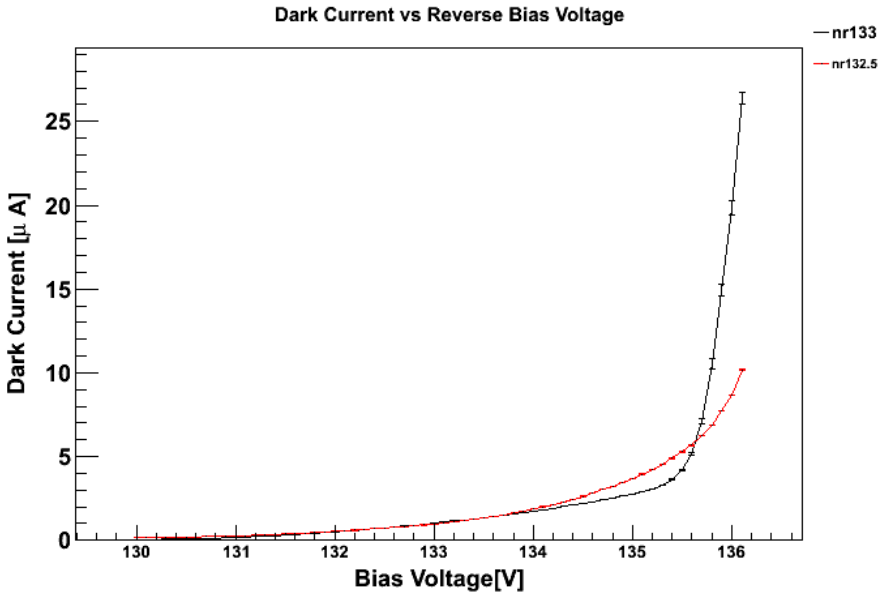


(a) MAPD

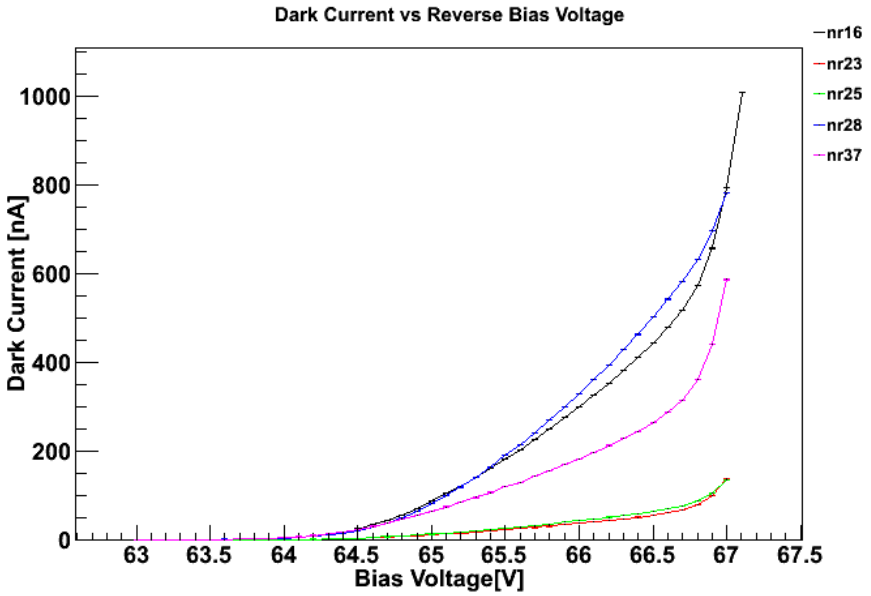


(b) MAPD3-A

Figure 5.5: The dark current as a function of the bias voltage for the different photodetectors.

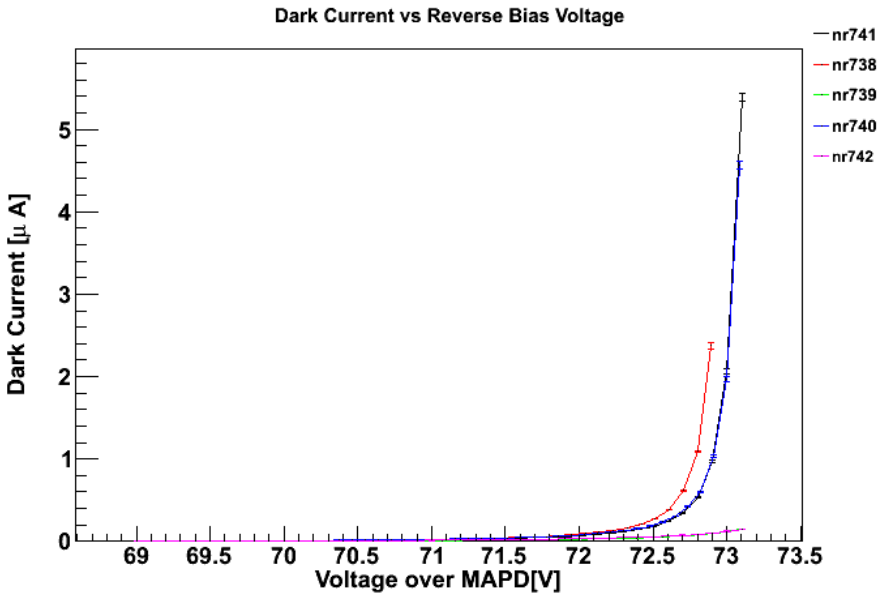


(a) MPPC S10362-11-25C

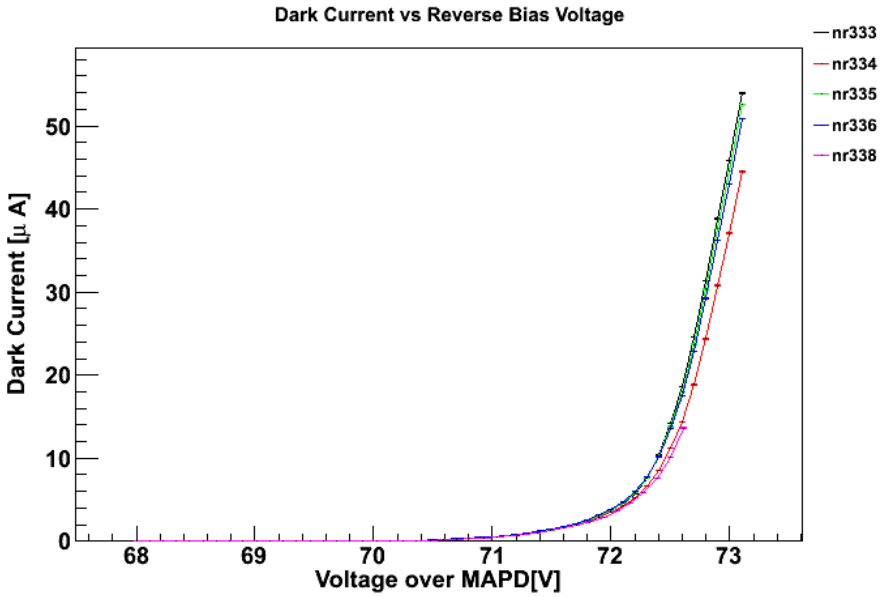


(b) MPPC S10362-33-50C

Figure 5.6: The dark current as a function of the bias voltage for different detectors.

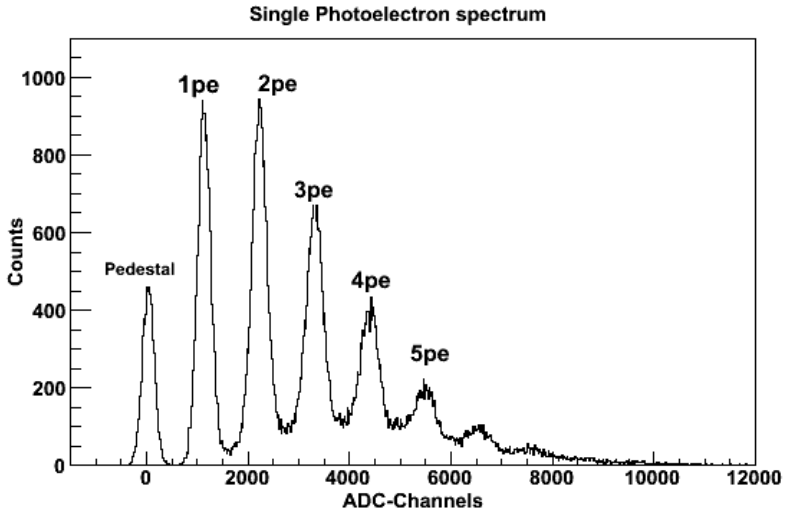


(a) MPPC S10362-11-25C, this is for sample 742

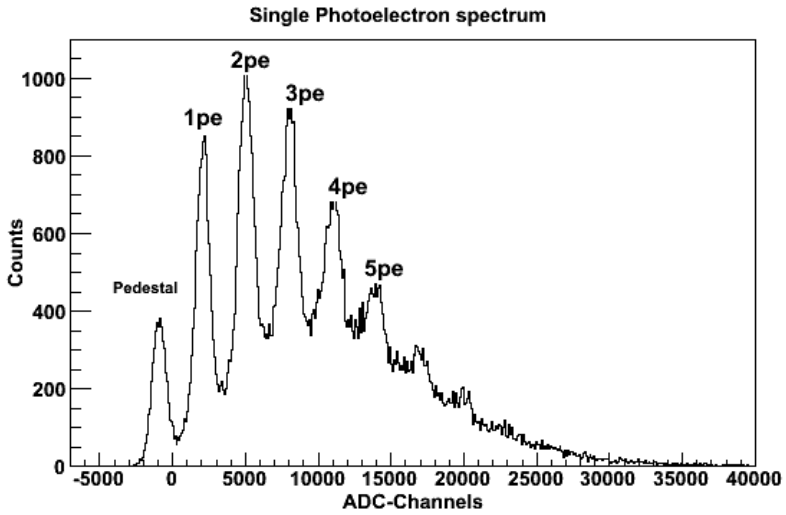


(b) MPPC S10362-33-50C, this is for sample 338

Figure 5.7: Typical plots for the single photoelectron spectrum for a fixed bias voltage, here used the recommended operating voltage for the specific device. The number of events is plotted versus the charge of the signal. The first peak corresponds to the pedestal peak (no photon is detected by the photodetector), second peak corresponds to the first photoelectron peak and so on.

types that has been tested. In both spectrums, the single photoelectron peaks can be seen very clearly, demonstrating an identical performance of the micro-cells and an excellent single photoelectron resolution of the different devices. The first peak corresponds to the pedestal peak, where the MAPD does not detect any photons. The second peak is the first photoelectron peak and so on. It can also be seen that the peaks for MPPC S10362-11-025C, Fig 5.7a, is less smeared out than the peaks for MPPC S10362-33-050C, Fig 5.7b. This can be understood from the fact that the capacitances for MPPC S10362-11-025C is smaller than for MPPC S10362-33-050C, which would introduce noise, see section 2.4. The dark rate is higher for these devices, as will be seen later. The afterpulsing of these devices is probably also higher, which could affect the spectrum as well. In addition, the gain is higher for the latter one, which makes them more vulnerable to temperature and voltage changes. It could also be that the capacitance values are not so uniform from pixel to pixel for these devices.

The single photoelectron spectrum can be used to calculate the gain for a specific bias voltage. The distance between two neighbouring peaks are needed for this. A Gaussian fit is applied to the pedestal and first photoelectron peak, and the difference between the mean values are found. To get a more accurate measurement of the gain this is done for all peaks, and an average value of the distances is obtained. The absolute gain can be found from the formula:

$$\text{Gain} = \frac{\text{Average distance peaks}}{\text{Gain}_{\text{preamp}} \cdot e} \quad . \tag{5.2}$$

As mentioned before, the gain of the preamplifier is 100.

Fig 5.8 shows the gain as a function of the bias voltage for the different detectors tested in this experiment. The distinction between the 2 different MPPC types can clearly be seen from this graph since the slopes of the two types differ significantly. Looking closer on the results for the MPPC S10362-11-025C, reveals a difference in gain for the same reverse bias voltages. This is to be expected since the recommended bias voltages given by Hamamatsu is higher for sample 739 and 742 than for the 3 others, indicating that also the breakdown voltage are higher for these two samples. When comparing the measured breakdown voltages, it can be seen that sample 739 and 742 has indeed a higher breakdown voltage than the rest, see Tab 5.2.

The gain shows a linear dependence on the bias voltage, as expected from Eq 2.8:

$$G = \frac{Q}{e} = \frac{C_{pixel}}{e}(V_{bias} - V_{breakdown}) \quad . \tag{5.3}$$

By applying a linear fit, G(V) = aV + b, to this curve, the pixel capacitance $C_{pixel}$ and the breakdown voltage $V_{breakdown}$ can be obtained from

$$C_{pixel} = a \cdot e, \quad V_{breakdown} = -\frac{b}{a} \quad . \tag{5.4}$$

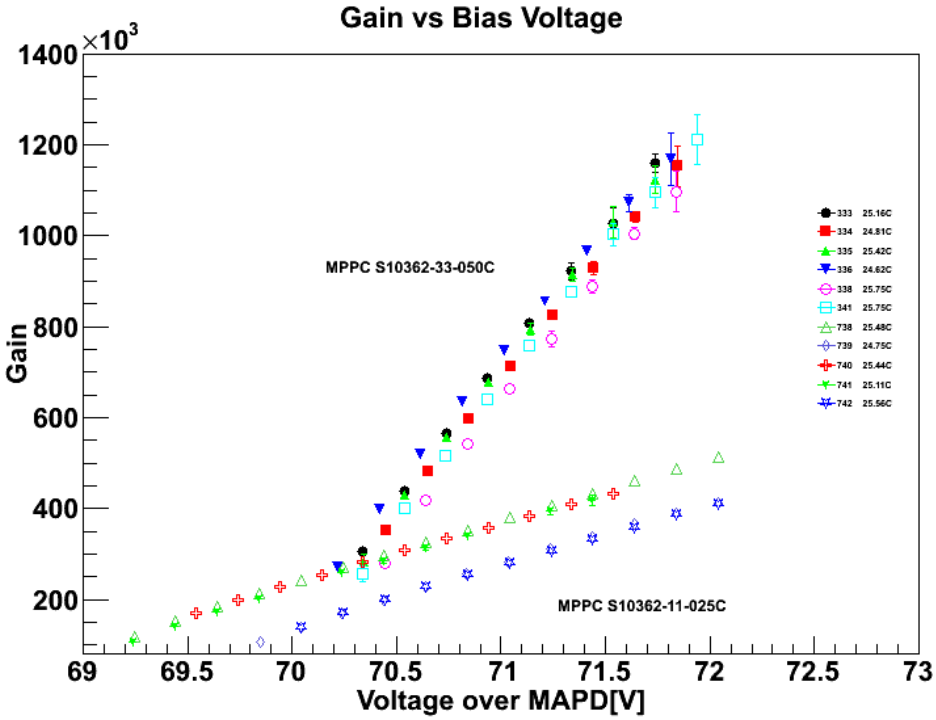


Figure 5.8: Gain as a function of bias voltage for all detectors tested. The temperature during the measurements is also given.

| Photodetector | $C_{pixel}$[fF] | $V_{breakdown}$ | %G/0.1V | %G/1$^o$C |
|---|---|---|---|---|
| MPPC S10362-33-050C | | | | |
| Sample333 | 98.5±1.7 | 69.83±1.70 | 7.07 | |
| Sample334 | 92.4±1.2 | 69.82±1.29 | 6.79 | -3.77 |
| Sample335 | 97.4±1.9 | 69.83±1.91 | 7.06 | -3.87 |
| Sample336 | 96.3±0.5 | 69.76±0.48 | 6.86 | |
| Sample338 | 97.1±1.4 | 69.96±1.48 | 7.14 | |
| Sample341 | 96.3±1.4 | 69.88±1.47 | 7.17 | -3.81 |
| MPPC S10362-11-025C | | | | |
| Sample738 | 22.29±0.15 | 68.31±0.65 | 4.35 | |
| Sample739 | 23.97±0.15 | 69.13±0.60 | 4.47 | |
| Sample740 | 21.73±0.30 | 68.28±1.34 | 4.24 | |
| Sample741 | 26.09±0.19 | 68.58±0.71 | 4.68 | -2.19 |
| Sample742 | 21.63±0.19 | 69.00±0.86 | 4.27 | -2.21 |

Table 5.2: Measured values of $C_{pixel}$, $V_{breakdown}$, the increase in gain when the voltage is increased by 0.1 V from recommended operating voltage and the decrease in gain when the temperature is increased from 24$^o$C - 25$^o$C.

The values a and b can further be used to find the increase in gain when increasing the bias voltage by 0.1 V. The "start"-value is for these calculations taken to be the recommended operating voltage, $V_{op}$, given by Hamamatsu. The increase in gain can be found from the formula

$$\frac{G(V_{op}+0.1)}{G(V_{op})} = \frac{a\cdot(V_{op}+0.1)+b}{aV_{op}+b} \quad . \tag{5.5}$$

Table 5.2 shows an overview of the measured values of $C_{pixel}$ and $V_{breakdown}$ for different detectors, plus the increase in gain for 0.1 V increase from the recommended bias voltage. In the linearity measurement, the amplitude of the signal as a function of the bias voltage was measured, Fig 5.9. It should be emphasized that this do not give the gain of these devices, the light intensity was too high for this, but it will give an idea of how the signal of the MAPD3-A responds when the reverse bias voltage is increased. From Fig 5.9 it can be seen that the amplitude versus the operating voltage is not linear. When the operating bias voltage is increased, there will be a higher electric field in the depletion region, and thus a higher probability for the incoming photon to trigger an avalanche. This can be a reason for the non-linearity.

When introducing the thermistor close to the MAPD for measuring the temperature dependence of the gain, this also introduced some noise. As mentioned earlier in this chapter, this noise was eventually removed.

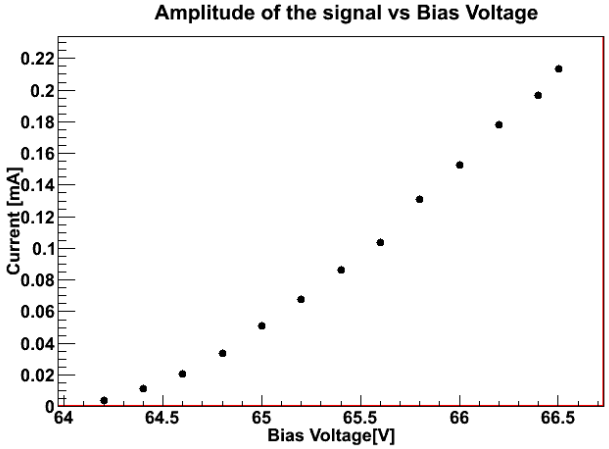


Figure 5.9: The amplitude of the signal as a function of the bias voltage over the MAPD3-A. These results are for the same MAPD3-A as in Fig 5.14

The gain and temperatures recorded are following plotted and fitted with a linear curve, Fig 5.10. As with gain versus voltage, a and b are extracted from the linear fit and used to find the decrease in gain when the temperature is increased with one degree from $24^o$C till $25^o$C using the formula:

$$\frac{G(25)}{G(24)} = \frac{a \cdot 25 + b}{a \cdot 24 + b} \quad . \tag{5.6}$$

The results for the devices that has been tested are shown in Tab 5.2.

The thermistor was first taped on top of the read-out circuit box. It was assumed that the temperature in the thermistor should be the same as the temperature in the MAPD. A problem with this is that the thermistor and the MAPDs seems to cool down and heat up a little differently. Still, it could be seen that the gain varies linearly with the temperature. To ensure that the temperature measured by the thermistor matched that of the MAPD, a copper plate were introduced. Holes were drilled into the copper to allow the feet of the MAPD to pass through, aligning the back of the MAPD with the copper plate. The thermistor was permanently connected to the copper, Fig 5.3. Thermal grease was applied to ensure good thermal conductivity between the copper, MAPD and thermistor. This improved the results, and it is now shown very clearly that the gain varies linearly with temperature, Fig 5.10.

Fig 5.11 shows the gain versus temperature for all detectors that have been tested. As the reverse bias voltage used for these measurements are the recommended bias voltage from Hamamatsu, it can be seen that the results are quite similar for each detector type. This is shown especially for MPPC 10362-11-025C, as these devices had the biggest differences in the

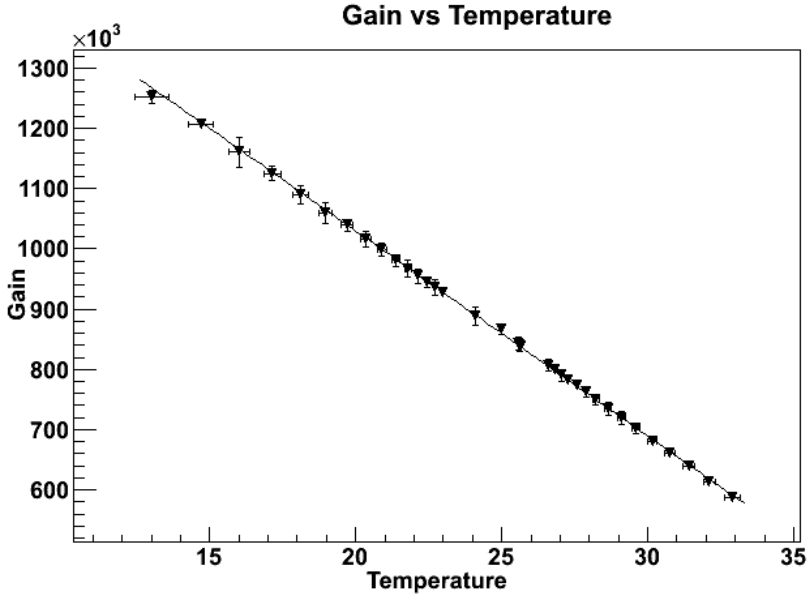


Figure 5.10: The gain versus temperature, here for for sample 341. A linear fit has been applied to illustrate the linear dependence of the gain on temperature.

recommended bias voltage. Sample 741 has a recommended bias voltage of 70.72 V, while sample 742 has 71.34 V, but the results are still very similar.

The technical datasheet given by Hamamatsu [37] shows the gain versus voltage and temperature, see appendix A. From this the gain dependence on voltage and temperature can be found. To calculate the gain versus voltage, a voltage of 71 V have been chosen as the operating voltage. This yielded an increase of 4% in gain when increasing the voltage with 0.1 V, which is in agreement with what has been measured, when also taking into account that the values in the datasheet is most likely an average value and that the individual detector values will fluctuate a bit. For the gain versus temperature, the decrease in gain when increasing the temperature from 24-25$^o$C was calculated from the technical datasheet to be around 2%. Again, in agreement with what has been measured.

## 5.4 Dark Rate

The Labview program, as mentioned, stored a text file with the pulse heights exceeding the 0.5pe threshold value. A ROOT program was now used to calculate the number of pulse heights, $N_{peaks}$, exceeding a specified threshold, starting from the 0.5pe threshold up to the highest pulse height recorded for the individual measurement. The frequency can be calculated using the

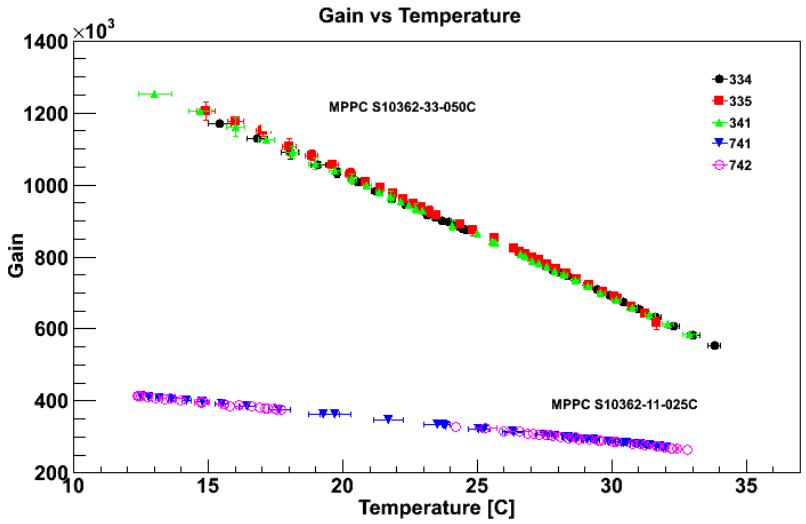


Figure 5.11: Gain versus temperature for the different detectors that has been tested. Because the measurements have been recorded with the recommended bias voltage for each detector, it can be seen that the different detectors within one detector type behaves quite similar. The different detector types can also be distinguished quite clearly.

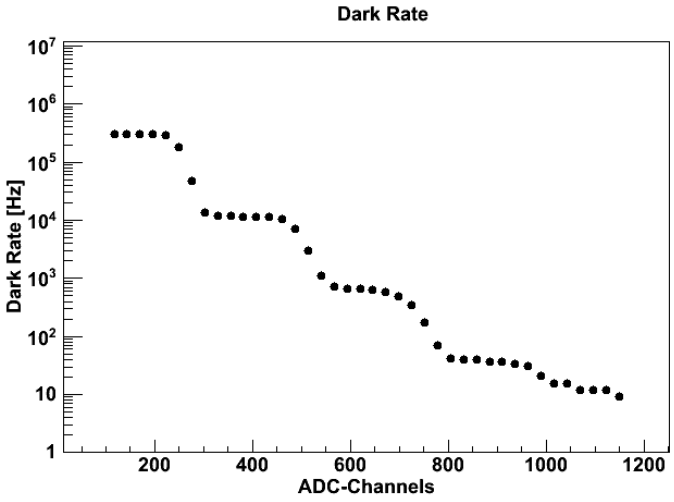


Figure 5.12: The dark rate for one of the MPPC S10362-11-025C, sample 742, for $V_{bias}$ = 71.44V. This graph shows that the dark rate is decreasing for increasing threshold.

formula

$$\text{Frequency} = \frac{\text{N}_{peaks}}{t_{tot}} \quad . \tag{5.7}$$

When Labview was triggered, it would read out memory, totalling 1260 ns. The total number of times it was triggered, $\text{n}_{triggered}$, was also counted and stored. This gives the total time, $\text{t}_{tot}$, for each dark rate measurement given by $\text{t}_{tot} = 1260 \text{ ns} \cdot \text{n}_{triggered}$.

Labview was programmed not to accept any peaks within 10 ns after a peak had been detected. This dead time, $\tau$, has to be corrected for, and this is done using the formula for dead time correction [3]

$$R = \frac{R'}{1 - R'\tau} \quad , \tag{5.8}$$

where R is the true rate and R' is the recorded rate.

The frequency versus threshold values for one of the MPPC S10362-11-025Cs are shown in figure 5.12. Here it is clearly shown that the dark rate is decreasing with an increasing threshold. This means that for high photon signals, the dark rate can be eliminated by setting an appropriate threshold value.

The dark rate for 0.5 pe threshold versus the reverse bias voltage for the different detectors, are shown in figure 5.13, showing as expected an increase of the dark rate with reverse bias voltage.

When the Labview program were looking for the peaks, it first averaged over a number of samples, which smoothed out the signal. Thus, the SNR of the signal was relative high, which made it easier for Labview to find the signal peaks. For MPPC-samples 334, 335, 336, 338 and 742 the parameters were a bit changed. The number of samples Labview averaged over, were reduced, making the SNR of the signal lower. The 0.5 threshold at low voltages for the MPPC S10362-33-050C was around 35-40 bins, which is lower than the $3 \cdot$ RMS that is normally used as a noise threshold. As Labview were just looking for bins which had a higher value than the threshold value, bins with high noise amplitude were recorded to be a dark rate signal. The detected dark rate got too high, and the dark rate at low operating voltages had to be taken away. Thus, in further dark rate measurements the signal should be averaged over to reduce the number of bins with high noise amplitude. In addition, the threshold used in Labview when looking for the peaks, should not be lower than the value $3 \cdot$ RMS value.

## 5.5 Linearity

In Labview, the amplitude and the charge, or integrated signal, were extracted. In Fig 5.14 they are plotted against the attenuation coefficients of the neutral density filters.

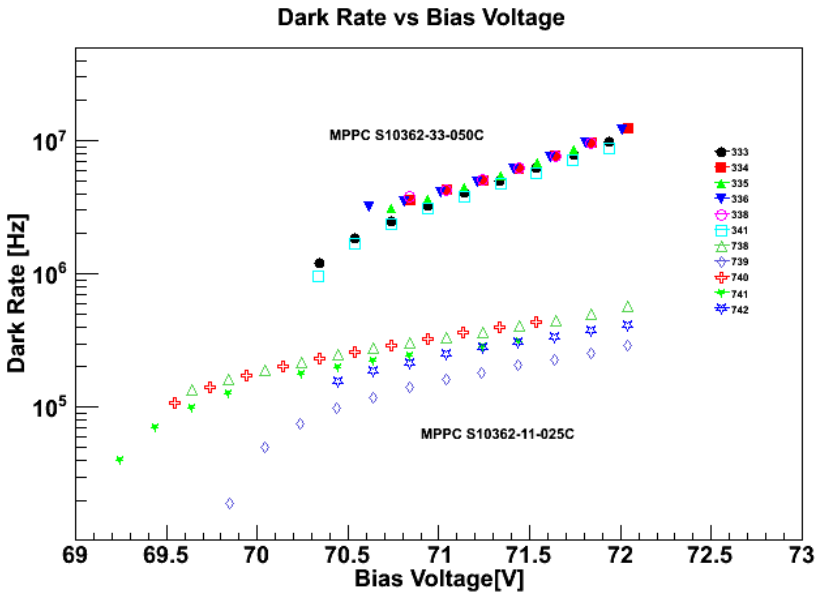


Figure 5.13: The dark rate as a function of bias voltage for 0.5pe threshold.

This setup is, however, not good enough for measuring the linearity. This can be seen in Fig 5.14, the results do not seem to be as linear as expected. This has to do with the light pulse that was employed. The width of the pulse was broader than the recovery time of the individual diode, and the risetime of the pulse was too long. Due to the broad pulse, late arriving photons could trigger already hit, but recovered cells and thus contribute to the signal. These linearity measurements were only done for some detector samples, as a new setup were proposed, but no yet tested.

## 5.6 Rise Time

Tab 5.1 shows the rise times recorded, while Fig 5.15 shows typical signal shapes for the different detectors. By looking at the signal shapes, it is seen very clearly that MPPC 10362-11-025C has a faster signal, the FWHM is much smaller. The rise times recorded for these detectors is also a little smaller. This can be understood from the capacitance for these devices, which is lower for MPPC 10362-11-025C. A smaller capacitance leads to a shorter time constant.

From the signal shape of sample 25, one of the MAPD3-A, the oscillations mentioned in section 5 can be seen. The conditions were the same for all detectors when taking the pictures, so this can indicate that the MAPD3-As are more susceptible to noise. As mentioned before, this was only discovered at the end of the measurements done for this thesis, so further investigations

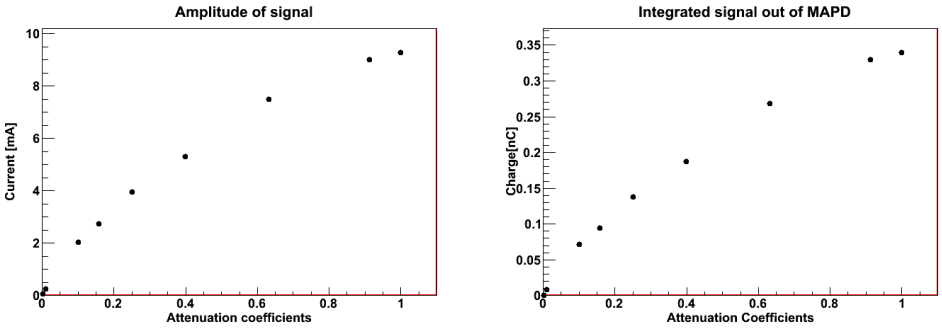


Figure 5.14: Left: Amplitude of the MAPD signal, Right: Charge of the MAPD signal, both as a function of the attenuation coefficients of the neutral density filters. These plots are for one of the MAPD3-As from Zecotek.

needs to be done. More shielding of the detector itself is probably a solution to prevent it from picking up noise from for instance the thermistor.

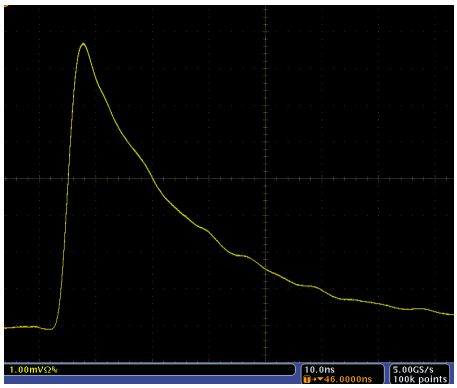

(a) MPPC 10362-33-050C, sample 341. X-axis: 10 ns, Y-axis: 1 mV

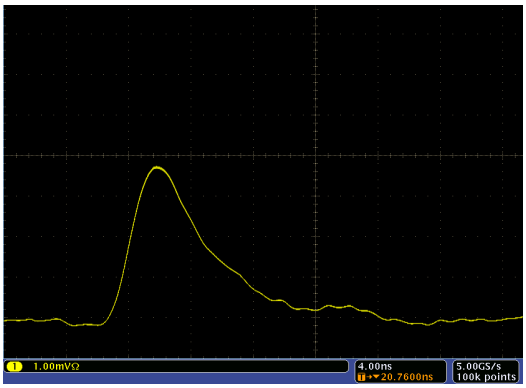

(b) MPPC 10362-11-025C, sample 741. X-axis: 4 ns, Y-axis: 1 mV

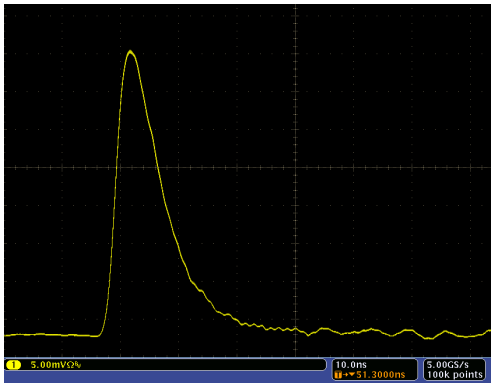

(c) MAPD, sample 133. X-axis: 10 ns, Y-axis: 5 mV

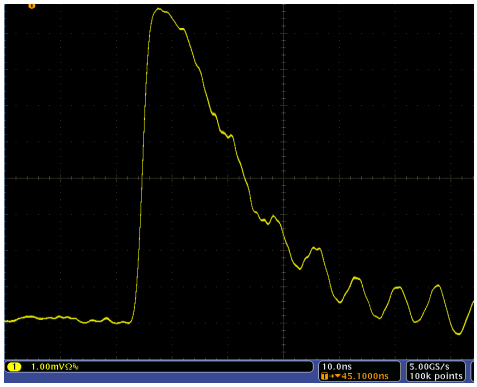

(d) MAPD3-A, sample 25. X-axis: 10 ns, Y-axis: 1 mV

Figure 5.15: Typical signal shape for the different types of detectors. Here it can clearly be seen that MPPC 10362-11-025C has a faster signal, the FWHM is much smaller than for the other 3.

# Chapter 6

# Conclusion and Outlook

This thesis has been focused on the characterization of Multipixel Avalanche Photodiodes (MAPDs). A characterization setup has been made, making it easy to characterize each individual photodetector with respect to dark current, dark rate and absolute gain. A lot of time has been spent to reduce noise in the system, but this is still something that can be improved.

The detectors that have been tested, range in among other things, gain and dynamical range. This makes them interesting for different applications. The high dynamical range makes the MAPDs from Dubna and Zecotek more applicable for hadron calorimeters. The Projectile Spectator Detector (PSD), which will be located at NA61/SHINE at CERN, is an example of this. The MultiPixel Photon Counters (MPPCs) from Hamamatsu have a lower dynamical range, but in return they have a higher gain. This makes them more suitable when detecting low energy photons, as in Positron Emission Tomography (PET).

The dark current has been tested for all four types, altogether 17 samples. The dark current increases exponentially for increasing reverse bias voltage, which makes it important not to set the bias voltage too high. As expected, the dark current is smallest for the MAPD3-As from Zecotek, as these detectors have the lowest gain. The dark current here ranges from 1-1000 nA. For the devices which have the highest gain, the MPPC 10362-33-050C, the dark current is also the largest, ranging from 1-50 $\mu$A.

The gain of 2 types of MultiPixel PhotonCounters (MPPC), altogether 11 samples, have been recorded over a variety of reverse bias voltages. The gain ranged between $(0.1\text{-}1.4)\cdot 10^6$, depending on the reverse bias voltage. When increasing the voltage by 0.1 V from the recommended bias voltage, the gain increased with around 7% or around 4.4% depending on the type of MPPC. The gain of the two MAPD types together with the preamplifier, is not high enough to be able to see single photons, the SNR for these devices is too low.

Due to instability of the gain recorded, the gain was also measured as

a function of the temperature. The gain decreases when the temperature increases due to an increase in the breakdown voltage. When increasing the temperature from 24 to 25$^o$C, the gain decreased by around 2.2% and 3.8% depending on the type of MPPC in question.

The dark rate has been recorded for the same samples as for the absolute gain. With a threshold of 0.5 of the pulse height of one photoelectron, the dark rate has been recorded to be between $10^4$ -$2{\cdot}10^7$Hz, depending on the reverse bias voltage. The dark rate has been found to be decreasing for increasing threshold, so for applications where the number of photons is high, the dark rate will not be important.

A measurement setup of the linearity was made, but due to a very broad light pulse with long risetime the measurements done here are not satisfactory. When the width of the pulse is too broad, late arriving photons can trigger a pixel that is already hit, but has had time to recover. A fast pulser has been made which produces a narrow pulse with short risetime. This should ensure that all photons hit the MAPD within the recovery time of the detector. The light from the Light Emitting Diode (LED) connected to the fast pulser will be guided to the MAPD using an optical fibre. This fibre will also split the light and lead the other part of the light signal to a PhotoMultiplier Tube (PMT), which will be used as a reference instead of using the neutral density filters. This is just a proposed setup and has not yet been tested.

The single photoelectron spectrum obtained when measuring the absolute gain, demonstrated the identical performance of the micro-pixels. It is still necessary to look into long term stability of the devices by measuring the gain over a long period of time, determine the uniformity of the MAPD and also to see how many dead pixels there are. For this use, a very precise laser is needed together with a very precise x-y table. The Photon Detection Efficiency (PDE) is also something that needs to be tested, to see which wavelenghts the photodetectors respond best to.

# List of Figures

# List of Tables

# Bibliography


[1] W.R. Leo. *Techniques for nuclear and particle physics experiments.* Springer-Verlag, 1987.

[2] C. Amsler et al. Passage of particles through matter. *Physics Letters*, B667, 2008.

[3] K. Kleinknecht. *Detectors for Particle Radiation.* Cambridge Univeristy Press, second edition, 1998.

[4] G.F. Knoll. *Radiation Detection and Measurement.* Johh Wiley and Sons Inc, third edition, 2000.

[5] G. Nelson and D. Reilly. Gamma-ray interaction with matter. http://www.sciencemadness.org/lanl1_a/lib-www/la-pubs/00326397.pdf.

[6] P.E. Valk et al. *Positron Emission Tomography, Basic Science and Clinical Practice.* Springer, 2003.

[7] C. Amsler et al. Particle detectors. *Physics Letters*, B667, 2008.

[8] S.A. Dyer. *Survey of Intrumentation and Measurement.* Wiley-IEEE, second edition, 2001.

[9] C. Grupen and B. Shwartz. *Particle Detectors (Cambridge Monographs on Particle Physics, Nuclear Physics and Cosmology).* Cambridge University Press, 2008.

[10] A. Yariv. *Optical Electronics.* Saunders College Publisher, fourth edition, 1991.

[11] H. Spieler. *Semiconductor Detector Systems.* Oxford Science Publications, 2005.

[12] I. Wegrzecka et al. Design and Properties of silicon avalanche photodiodes. *Opto-electronics review*, 12(1):95–104, 2004.

[13] B.F. Aull et al. Geiger-Mode Avalanche Photodiodes for Three-Dimensional Imaging. 2002.

[14] Y. Musienkoa et al. A simple model of EG & G reverse reach-through APDs. *Nuclear Instruments and Methods in Physics Research Section A: Accelerators, Spectrometers, Detectors and Associated Equipment*, 442(1-3):179 – 186, 2000.

[15] N. Otte. The Silicon Photomultiplier: A New Device for High Energy Physics, Astroparticle Physics, Industrial and Medical Applications. In the Proceedings of International Symposium on Detector Development for Particle, Astroparticle and Synchrotron Radiation Experiments (SNIC 2006), Menlo Park, California, 3-6 Apr 2006.

[16] V.D. Kovaltchouk et al. Comparison of a silicon photomultiplier to a traditional vacuum photomultiplier. *Nuclear Instruments and Methods in Physics Research Section A: Accelerators, Spectrometers, Detectors and Associated Equipment*, 538(1-3):408 – 415, 2005.

[17] A. Tadday. Characterization of silicon photomultipliers. Master's thesis, Kirchhoff-Institut fur Physik, 2008.

[18] P. Buzhan et al. An advanced study of silicon photomultiplier. 2001. Talk Given at the International Conference on Advanced Technology and Particle Physics, Como, Italy.

[19] V. Golovin and V. Saveliev. Novel type of avalanche photodetector with Geiger mode operation. *Nuclear Instruments and Methods in Physics Research Section A: Accelerators, Spectrometers, Detectors and Associated Equipment*, 518(1-2):560 – 564, 2004. Frontier Detectors for Frontier Physics: Proceedings.

[20] Z.Z. Sadygov. Three advanced designs of avalanche micro-pixel photodiodes. June 2005. Talk given at the International Conference, Beaune, France.

[21] Z. Sadygov et al. Three advanced designs of micro-pixel avalanche photodiodes: Their present status, maximum possibilities and limitations. *Nuclear Instruments and Methods in Physics Research Section A: Accelerators, Spectrometers, Detectors and Associated Equipment*, 567(1):70 – 73, 2006. Proceedings of the 4th International Conference on New Developments in Photodetection - BEAUNE 2005, Fourth International Conference on New Developments in Photodetection.

[22] S. Cova et al. Avalanche photodiodes and quenching circuits for single-photon detection. 1996.

[23] H.G. Moser. Silicon detector systems in high energy physics. *Progress in Particle and Nuclear Physics*, 63(1):186 – 237, 2009.

[24] A.L Lacaita et al. On the bremsstrahlung origin of hot-carrier-induced photons in silicon devices. *Electron Devices, IEEE Transactions on*, 40(3):577–582, Mar 1993.

[25] A. G. Chynoweth and K. G. McKay. Photon Emission from Avalanche Breakdown in Silicon. *Physical Review*, 102:369–376, April 1956.

[26] F. Guber et al. Very Forward Hadron Calorimeter for the CBM Experiment- Projectile Spectator Detector(PSD). 2006.

[27] M. Golubeva et al. Longitudinally segmented lead/scintillator hadron calorimeter with micro-pixel APD readout. *Nuclear Instruments and Methods in Physics Research Section A: Accelerators, Spectrometers, Detectors and Associated Equipment*, 598(1):268 – 269, 2009. Instrumentation for Collding Beam Physics - Proceedings of the 10th International Conference on Instrumentation for Colliding Beam Physics.

[28] M. Golubeva et al. Proposal Development and construction of the Projectile Spectator Detector for the NA61 experiment. october 2007.

[29] W.W. Moses. Synergies between electromagnetic calorimetry and PET. (LBNL–51197), 2002.

[30] W.W. Moses. Advantages of improved timing accuracy in PET cameras using LSO scintillator. volume 3, pages 1670–1675 vol.3, Nov. 2002.

[31] J.S. Karp et al. Benefit of time-of-flight in pet: Experimental and clinical results. 2008.

[32] J.S. Karp. Time-of-flight pet. *SNM*, 3, 2006.

[33] K. Wienhard. Positron Emission Tomography. 2007.

[34] M. Conti et al. First experimental results of time-of-flight reconstruction on an lso pet scanner. 1978.

[35] R. Brun and F. Rademakers. ROOT - An Object Oriented Data Analysis Framework. Proceedings AIHENP'96 Workshop, Lausanne, Sept 1996, Nucl. Inst. & Meth. in Phys. Res. A 389 (1997) 81-86. See also http://root.cern.ch/.

[36] O. Veledar et al. Simple techniques for generating nanosecond blue light pulses from light emitting diodes. *Measurement Science and Technology*, 18(1):131–137, 2007.

[37] Hamamatsu. *Technical Information: The Multi-Pixel Photon Counter*, January 2003.

# Appendix A

# MPPC specifications

The recommended operating voltage that Hamamatsu has given for each individual detector is given in Tab A.1. In addition, the gain and dark rate for 0.5 threshold and 1.5 threshold at the recommended operating voltage and a temperature of 25$^o$C is given.

The recommended operating voltage at 25$^o$C and the gain, 0.5threshold and 1.5threshold at 25$^o$C at this voltage and temperature that Hamamatsu has given for each individual detector, is given in table A.1.

| Detector | $V_{op}$ [V] | Gain [$10^5$] | 0.5thr [Hz] | 1.5thr [Hz] |
|---|---|---|---|---|
| MPPC S10362-33-050C | | | | |
| Sample 333 | 71.24 | 7.50 | 3.91M | 0.69M |
| Sample 334 | 71.29 | 7.50 | 4.3M | 0.82M |
| Sample 335 | 71.25 | 7.50 | 4.18M | 0.73M |
| Sample 336 | 71.22 | 7.50 | 4.1M | 0.77M |
| Sample 338 | 71.36 | 7.50 | 4.56M | 0.92M |
| Sample 341 | 71.27 | 7.50 | 3.93M | 0.68M |
| MPPC S10362-11-025C | | | | |
| Sample 738 | 70.61 | 2.75 | 291K | 8.31K |
| Sample 739 | 71.37 | 2.76 | 236K | 5.34K |
| Sample 740 | 70.64 | 2.75 | 307K | 7.54K |
| Sample 741 | 70.72 | 2.75 | 274K | 6.21K |
| Sample 742 | 71.34 | 2.75 | 287K | 7.91K |

Table A.1: The recommended voltage for each individual detector, plus the gain, 0.5 threshold and 1.5 threshold for the dark rate at this voltage. All of these are for a temperature of 25$^o$C.

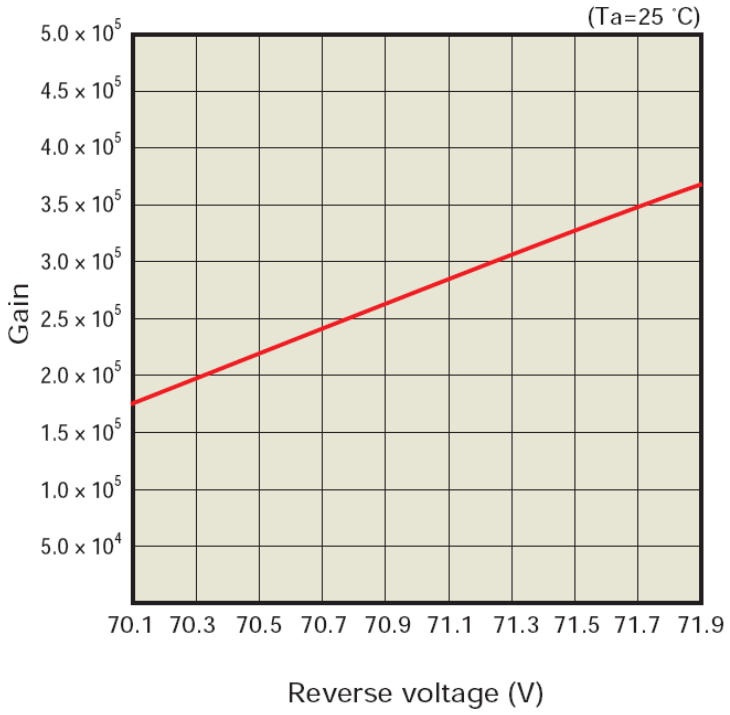
(Ta=25 ˚C)
Gain
5.0 × 10^5
4.5 × 10^5
4.0 × 10^5
3.5 × 10^5
3.0 × 10^5
2.5 × 10^5
2.0 × 10^5
1.5 × 10^5
1.0 × 10^5
5.0 × 10^4
70.1 70.3 70.5 70.7 70.9 71.1 71.3 71.5 71.7 71.9
Reverse voltage (V)

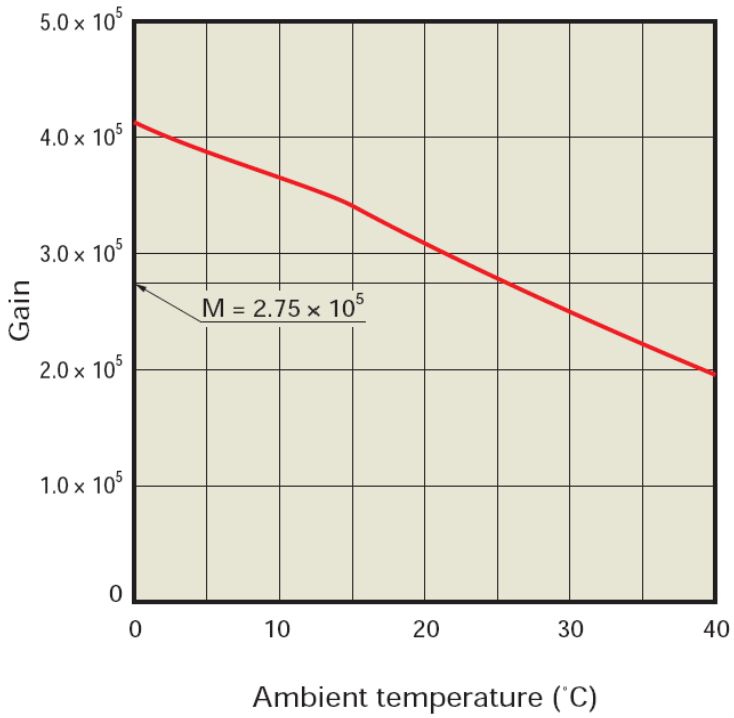
Gain
5.0 × 10^5
4.0 × 10^5
3.0 × 10^5
2.0 × 10^5
1.0 × 10^5
0
M = 2.75 × 10^5
0 10 20 30 40
Ambient temperature (˚C)

| Parameter | S10362-11-025C | S10362-33-050C |
|---|---|---|
| Chip size [mm] | 1.5x1.5 | 3.5x3.5 |
| Effective active area[mm] | 1x1 | 3x3 |
| Number of pixels | 1600 | 3600 |
| Pixel Size [$\mu$m] | 25x25 | 50x50 |
| Fill Factor [in %] | 30.8 | 61.8 |
| Spectral response range, $\lambda$ [nm] | 270 to 900 | 270 to 900 |
| Peak sensitivity wavelength, $\lambda_p$] [nm] | 400 | 400 |
| Quantum efficiency, $Q_E$ [%] | 70min | 70min |
| Photon Detection Efficiency, PDE [%] | 25 | |
| Dark Count [kcps] | 300 | 3 |
| Dark Count$_{max}$ [kcps] | 600 | 5 |
| Terminal capacitance $C_t$ [pF] | 200-300 | - |
| Time resolution (FWHM)[ps] | 35 | 320 |
| Gain, M | 2.75 x $10^5$ | 7.5x $10^5$ |

# Appendix B

# MAPD Specifications

The following figures lists the characteristics given by Dubna:

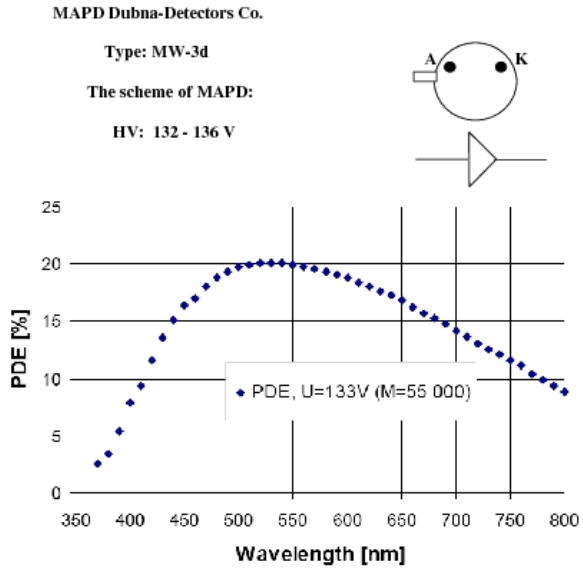


Fig.1 Dependence of Photon Detection Efficiency (PDE) on light wavelength.

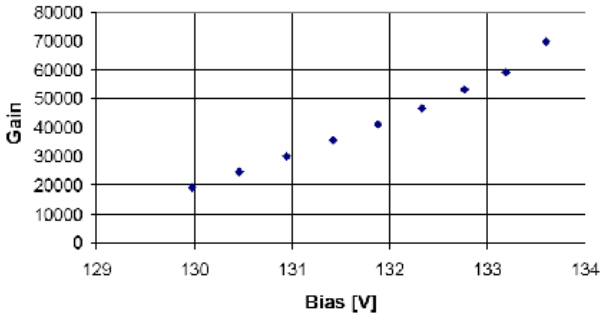


Fig.2 Dependence of Gain on bias HV.

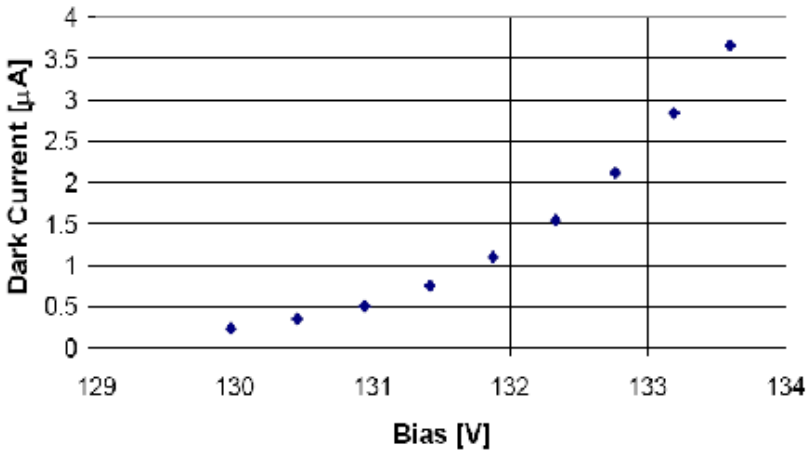


Fig.2 Dependence of Dark Current on bias HV.

These MAPDs have $10^4$ pixels/mm$^2$ that provides a nice dynamical range.
They must be operated in inverse direction: Anode should be grounded, while positive voltage in range 132-136 V must be applied to cathode. Maximum gain $<10^5$ needs an additional amplification for a factor 100.
Exceeding the voltage 137 V leads to the unstable operation and even to the destruction of MAPD.